The EarthCARE lidar cloud and aerosol profile processor (A-PRO): the A-AER, A-EBD, A-TC and A-ICE products

David Patrick Donovan[1], Gerd-Jan van Zadelhoff[1], and Ping Wang[1]

[1]Royal Netherlands Meteorological Institute (KNMI), de Bilt, the Netherlands

Correspondence: D.P. Donovan (donovan@knmi.nl)

Abstract. ATLID ("ATmospheric LIDar") is the lidar to be flown on the multi-instrument Earth Clouds and Radiation Explorer (EarthCARE). EarthCARE is a joint ESA/JAXA mission now scheduled for launch in 2024. ATID is a 3 channel linearly polarized High-Spectral Resolution (HSRL) system operating at 355 nm. Cloud and aerosol optical properties are key EarthCARE products. This paper will provide an overview of the ATLID L2a (i.e. single instrument) retrieval algorithms being developed and implemented in order to derive cloud and aerosol optical properties. The L2a lidar algorithms that retrieve the aerosol and cloud optical property profiles and classify the detected targets are grouped together in the so-called A-PRO (ATLID-profile) processor. The A-PRO processor produces the ATLID L2a Aerosol product (A-AER), the Extinction, Bakscatter and Depolarization product (A-EBD), the ATLID L2a Target Classification (A-TC), and the ATLID L2a Ice microphysical estimation product (A-ICE). This paper provides and overview of the processor and its component algorithms.

1 Introduction

This document describes the algorithms within the EarthCARE (Illingworth et al., 2015) L2a Lidar Extinction, Backscatter and Depolarization L2a processor (A-PRO). Within the EarthCARE project, single-instrument geophysical property retrievals are referred to as L2a retrievals. A-PRO has been developed with support from the European Space Agency (ESA) for specific application to the EarthCARE lidar ATmospheric LIdar (ATLID) (do Carmo et al., 2021) and comprises a number of new developments. Within this processor, four main sub-algorithms exist, a procedure aimed at deriving the large-scale aerosol (and thin cloud) extinction and backscatter (A-AER), an optimal estimation based Extinction and Backscatter retrieval algorithm (A-EBD), a lidar target classification procedure (A-TC) and an ice microphysical property estimation procedure (A-ICE). Output products corresponding to each of these component procedures are generated. Collectively, these algorithms produce multi-horizontal-resolution profiles of lidar extinction, backscatter, optical depth, particle type, ice effective radius, ice water content as well as target type (e.g. cloud phase, aerosol-type etc.). This paper presents the theoretical background of the algorithms that comprise the A-PRO processor as well as presenting and discussing various examples. The examples shown are based on the simulations described in Donovan et al. (2023).

1.1 ATLID

ATLID is a linearly polarized three channel lidar operating at 355nm. The vertical resolution of the return signal is about
100 m throughout most of the atmosphere. The pulse-repetition-frequency (PRF) is 51 Hz and nominally it is planned that
two shots will be averaged on-board giving a horizontal resolution on the order of 305 m. The lidar delivers profiles of the
co-polarized Mie (or particulate) attenuated backscatter, the parallel Rayleigh (molecular) attenuated backscatter and the Mie
cross-polarized return.

ATLID is a so-called High Spectral Resolution Lidar (HSRL) Eloranta (2005). In the case of ATLID, a Fabry-Pérot Etalon
is used to (imperfectly) separate the spectrally narrow return from aerosols and clouds ('Mie') from the thermally broadened
return from atmospheric molecules ('Rayleigh'). Note that Mie scattering, properly, refers only to scattering by perfect spheres.
In this paper (and indeed through much of EarthCARE related documentation) we use the term rather loosely to broadly cover
what should be termed 'particulate' scattering. Further, the term 'Rayleigh' scattering is also used loosely. A more accurate term
would be 'molecular' or 'Rayleigh-Brillouin' scattering. Since the Rayleigh and Mie signal separation is imperfect a degree
of 'cross-talk' between the channels exists. In order to separately quantify the pure Mie and Rayleigh scattering contributions
a cross-talk correction procedure is applied as part of the L1 processing. ATLID emits linearly polarized light and separates
the returned backscatter in components polarized parallel and perpendicular to the plane defined by the emitted beam. The
polarization separation comes before the HSRL spectral filter. Accordingly, the three ATLID channels are:

- A parallel (or co-polar) Mie channel.

- A parallel (or co-polar) Rayleigh Channel.

- A perpendicular (or cross-polar) combined Mie and Rayleigh Channel.

ATLID is described in more detail within do Carmo et al. (2016) and do Carmo et al. (2021).

After spectral and polarization cross-talk correction and calibration, the ATLID backscatter signals can be related to the
atmospheric extinction and backscatters (neglecting multiple-scattering effects for the time being) as:

$$b_R(z) = p_R(z)r(z)^2 = \beta_R(z) \exp\left[-2 \int_{z_{lid}}^{z} (\alpha_M(z') + \alpha_R(z'))dr(z')\right] \tag{1}$$

$$b_{M,\parallel}(z) = p_{M,\parallel}(z)r(z)^2 = \beta_{M,\parallel}(z) \exp\left[-2 \int_{z_{lid}}^{z} (\alpha_M(z') + \alpha_R(z'))dr(z')\right] \tag{2}$$

$$b_{M,\perp}(z) = p_{M,\perp}(z)r(z)^2 = \beta_{M,\perp} \exp\left[-2 \int_{z_{lid}}^{z} (\alpha_M(z') + \alpha_R(z'))dr(z')\right] \tag{3}$$

Where b_R is the Rayleigh attenuated backscatter, $b_{M,\parallel}$ is the co-polar Mie attenuated backscatter, $b_{M,\perp}$ is the cross-polar Mie
attenuated backscatter, z is the atmospheric altitude and $r(z)$ is the range from the lidar. α_M is the aerosol and cloud extinction

and α_R is the atmospheric Rayleigh extinction. $\beta_{M,\parallel}$ is the co-polar Mie backscatter, β_R is the Rayleigh backscatter, and $\beta_{M,\perp}$ is the cross-polar Mie backscatter. Referring to Eqs. (2) and (3) the total Mie scattering is given by

$$b_M = b_{M,\parallel} + b_{M,\perp} \tag{4}$$

55   The primary function of this processor is to invert the lidar signals to obtain estimates of backscatter and extinction, and using these values together with the particle linear depolarization ratio ($\delta_M = \left(\beta_{M,\perp}/\beta_{M,\parallel}\right) = \left(b_{M,\perp}/b_{M,\parallel}\right)$) in order to classify the detected targets.

1.2   Multiple-scattering model

In general, for space-based lidars multiple-scattering can be an importance contribution to the detected signals and must be
60   accounted for (Winker, 2003). In this work, a novel approach has been used which lies in terms of speed and accuracy between the simple effective extinction approach due to Platt (Platt, 1981) and the approach of Hogan (Hogan, 2008). The multiple scattering formalism used in this work is detailed in Appendix B.

2   A-PRO retrieval processor

In principle, HSRL retrievals can yield direct estimates of extinction and backscatter profiles (Eloranta, 2005), however, the
65   direct method for estimating the backscatter involves calculating the ratio of the Mie (Eqs.(2,3)) and Rayleigh (Eq.(1)) signals while the extinction estimation involves taking the derivative of the logarithm of the Rayleigh signal Eq. (1) with range. Both these mathematical operations are sensitive to noise, particularly when small (or even possibly) negative values may be present in the Rayleigh channel. Thus, direct inversions are only practical when the data is of a suitably high Signal-to-Noise ratio (SNR).

70   The SNR of the attenuated HSRL backscatter signals can be increased by along-track averaging of the signals. However, this can produce, at best, biased, and at worst, ambiguous or non-physical results, if, for example, 'strong' (e.g. cloud) and 'weak' signals are averaged indiscriminately together. Thus, any averaging of the signals must respect the structure of the atmospheric scene being probed. Aerosol fields may be homogeneous enough and the signals weak enough that averaging along track for several 10's of km may be justified. On the other hand, cloud returns may be strong and inhomogeneous to the point that it is
75   desirable to apply inversions on the finest available resolution.

What is required is a means to guide the averaging the signals when appropriate and a multi-scale approach for retrieving optical properties and target classification for both aerosols and clouds. The A-PRO processor structure is designed with such goals in mind.

2.1   General structure

80   A-PRO is divided into three main algorithms as depicted in Fig. 1.
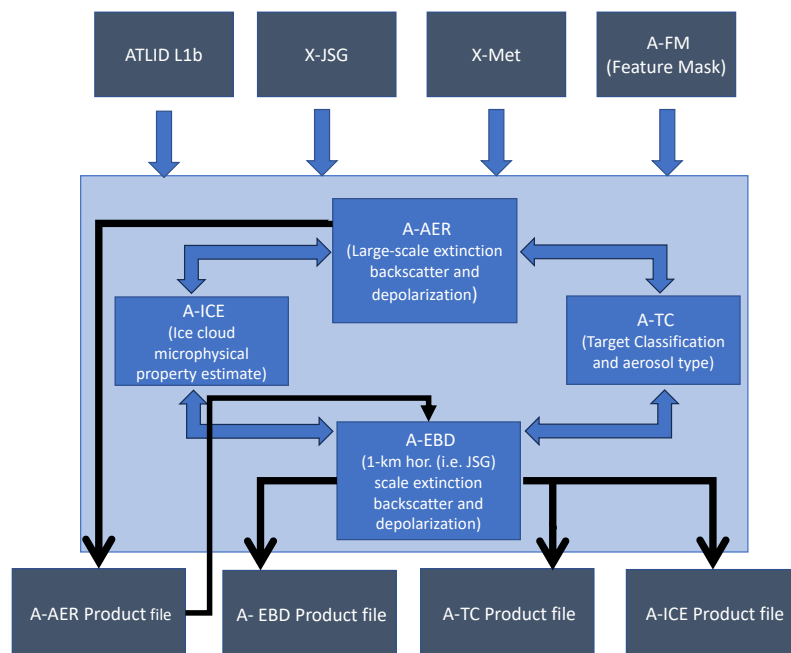
The main inputs to A-PRO are:

Figure 1. Schematic depiction of the high-level structure of the A-PRO processor. The top dark-Grey boxes represent the input products while the bottom dark-Grey boxes represent the output products. The double-headed arrows are used to indicate that the data-flow is bi-directional between the main procedures (A-AER and A-EBD) and the A-ICE and A-TC related procedures.

L1 ATLID product Calibrated cross-talk corrected attenuated backscatter profiles.

X-JSG Auxiliary data product The Joint Standard grid product facilitates the co-location of the EarthCARE L2 products with one and other (Eisinger et al., 2022).

85 **X-MET Auxiliary data product** X-MET contains the atmospheric pressure, temperature, etc.. build using ECMWF forecast data (Eisinger et al., 2022).

A-FM L2 product The ATLID Feature-Mask provides a high-resolution mask of detected targets. The use of A-FM helps facilitate the appropriate averaging of the data. A-FM uses a combination of image processing techniques in order to identify regions of clouds/aerosols, surface returns, clear air, or attenuated regions. The detected aerosol/cloud regions

90 are separated into cloud phase and aerosol type later in subsequent processing steps. Details of A-FM can be found in van Zadelhoff et al. (2023)

Within A-PRO the following main procedures are present.

Aerosol oriented extinction and backscatter retrieval (A-AER) This procedure uses direct HRSL retrieval methods for determining extinction and backscatter at the 50km+ horizontal scale (e.g. deriving the extinction based on the log-

95 derivative of the Rayleigh signal (Eloranta, 2005)). In order to do this the lidar signals must be appropriately masked

and averaged to achieve a target SNR. The averaging mask originates from the A-FM output which is used to avoid averaging "strong" and "weak" features together. The methods used by A-AER to estimate extinction and backscatter are described in Section 2.2 and Appendix A.

Cloud and aerosol Extinction, Backscatter and Depolarization procedure (A-EBD) This routine retrieves the aerosol and cloud extinction and backscatter profiles at the 1-km horizontal scale. At this scale, the SNR of the molecular scattering channel return is too low to enable the techniques employed by the A-AER approach. Instead, the method relies on a forward-modelling Optimal Estimation (OE) approach. As a-priori information, the lidar-ratio (S) estimates produced by A-AER are used as inputs in A-EBD.

Target classification procedure (A-TC) A-TC uses extinction, backscatter and depolarization ratio, as well as auxiliary inputs such as ECMWF forecast temperature, in order to classify targets into classes such as water or ice cloud or aerosol type. The aerosol typing scheme is based primarily on using the S and particle depolarization ratio to assign the aerosol to a type (Wandinger et al., 2023) . The cloud phase determination scheme uses layer integrated backscatter and depolarization in a manner similar to that employed for the CALIOP retrievals (Hu et al., 2009).

Ice Microphysical property Estimation (A-ICE) A-ICE employs a simple approach for estimating ice cloud effective radius and ice-water content (IWC) using the estimated extinction. In particular a parameterization which uses temperature and measured extinction is employed (Heymsfield et al., 2014a).

The above components work in a cooperative fashion. A-AER provides a first-pass focusing on the optically thin targets and A-EBD performs another pass to retrieve both the optically thick and thin targets using A-AER output as input. A-TC and A-ICE procedures are called by both A-AER and A-EBD.

2.2 A-AER

The A-AER procedure retrieves the large-scale optical properties of the optically thin regions ("weak-features") and "sets the stage" for the high resolution A-EBD stage of the A-PRO procedure.

A high-level depiction of the main elements of the A-AER procedure is presented in Figure 2. The inputs are the L1b ATLID data (attenuated cross-talk corrected backscatters for the three ATLID channels, the ATLID featuremask (A-FM) product (van Zadelhoff et al., 2023) and the auxiliary X-JSG (Joint standard Grid multi-instrument grid definition) and X-MET (ECMWF supplied meteorological fields) products (Eisinger et al., 2022).

The **first step** is to rebin the L1 ATBs to the JSG grid. At the same time, the associated errors in the ATB profiles are generated either by calculating the standard deviation of the ATBs or quadraticly summing the error estimates coming from the ATLID L1 product. A-FM data which is at native ATLID resolution is also put onto the JSG. In the case of the A-FM data the A-FM feature probability indices, are not averaged. Rather, the highest index within the appropriate JSG pixel is used, except in the case where the input indices contain a surface detection indication, in this case, the JSG pixel is flagged as a surface

pixel. As well, in this step, the temperature, pressure and atmospheric number density for each JSG pixel are determined using the X-MET auxiliary product.

The **2nd** step is to create a mask to guide the horizontal averaging of the input ATBs. A "strong feature" mask is created by thresholding the JSG-gridded A-FM product. This mask is then used in Step 3 to smooth the data respecting the mask.

In **Step 3**, the JSG-gridded ATBs are averaged using a moving average box-car, but pixels identified as "strong-features" are masked i.e. they are not considered in the averaging operation. The strong-feature pixels are then merged with the smoothed "weak-signals". The strong-feature A-FM threshold and the averaging window are both configurable. The pre-launch defaults are set to ≥ 8 for the A-FM threshold and 1 vertical range-gate by 40 horizontal JSG pixels for the averaging window. The setting of these configuration parameters, along with any others, will be re-evaluated during commissioning phase (and indeed throughout the mission life-time) on the basis of real observations.

In **Step 4** the lidar scattering ratio, i.e.

$$R(z) = \frac{\beta_{Mie}(z) + \beta_{Ray}(z)}{\beta_{Ray}(z)} = \frac{b_M(z) + b_R(z)}{b_R}, \tag{5}$$

is calculated along with corresponding error estimates using the ATBs resulting from the previous step. These scattering ratio estimates are then used, along with the JSG gridded A-FM data in step 5. In **Step 5** a "clear-sky' threshold is applied to the A-FM data, and on a column-by-column basis, the preliminary layering structure is determined. The scattering ratio calculations performed in the previous step along with the temperature fields. This process is described in detail in Irbah et al. (2023). In brief, layer boundaries are assigned whenever significant changes in the JSG A-FM indices or, optionally, significant temperature and scattering ratio are encountered.

In **Step 6**, the altitude dependent limits that will be applied on a column-by-column basis in order to average the ATBs in preparation for the quantitative determination of extinction and backscatter are found. The first sub-step is to define a mask representing pixels where it is considered valid to average over horizontally. This mask is first built by masking out

– Fully attenuated pixels.

– Surface Pixels

– Pixels with an associated value the JSG-gridded FM above a set threshold e.g. 7.

– Pixels with an associated scattering ratio (as calculated in Step 4) above a set threshold e.g. 5.

Averaging attenuated regions (e.g. below significant clouds) together with unattenuated regions would ultimately lead to inaccurate extinction and backscatter profiles. In order to avoid this, the averaging mask is set to false for that all altitudes in each respective column that are below the highest altitude of the mask in the given column. In addition, single pixel isolated true mask values (i.e. a true value completely surrounded by false values) are set to false.

The height-and-time dependent horizontal averaging limits are then found. This is accomplished by first considering a box centered around the JSG column in question. Then using all the data identified by the averaging mask the height averaged SNR of the resulting horizontally averaged Rayleigh ATB is calculated. If this average SNR is below a set threshold (e.g. 50) then

the horizontal extent of the box is expanded until the threshold is met or a specific maximum box extent is reached. The average

160 weak-feature ATBs for all three channels and their respective error estimates are then calculated (**Step 7**) for each height bin.

In **Step 8**, the weak-feature ATBs corrected for the effects of Rayleigh transmission (and in the case of the Rayleigh signal divided by the molecular backscatter) are smoothed vertically using a sliding linear least-square fitting procedure. The fitting window is configurable (e.g. 5 vertical range-bins). The use of a linear fit provides a natural way to handle the edge-effects at the top altitudes and the near ground-pixels i.e. linear extrapolation is used to find appropriate values of the pixels closer

165 than the fitting window half-width from the top of the profile or the ground-pixel. The use of a sliding linear fit provides also enables the range derivative of the signals to be calculated in the same step in a consistent manner. This procedure produces the *horizontally and vertically and smoothed* signals. Accordingly, we have:

$$B_{M,\parallel,hv} = F_{hv}\left(b_{M,\parallel}\exp[2\tau_{Ray}]\right), \tag{6}$$

170 $$B_{M,\perp,hv} = F_{hv}\left(b_{M,\perp}\exp[2\tau_{Ray}]\right), \tag{7}$$

and

$$B_{R,hv}^{Rat} = F_{hv}\left(\frac{b_R}{\beta_R}\exp[2\tau_{Ray}]\right). \tag{8}$$

where the Rat superscript is used to denote the fact that the ratio between the observed Rayleigh extinction corrected attenuated Rayleigh backscatter and the unattenuated Rayleigh backscatter is being calculated.

175 In Eqs. (6–8), F_{hv} is used to denote the masked vertical and horizontal smoothing operation, and τ_{Ray} is the Rayleigh optical depth from the Top-of-Atmosphere to the height in question. Here, for simplicity the range dependence is not written explicitly.

Step 9 involves the estimation of the particulate lidar-ratio S, the extinction and the backscatter. Depending on the configuration, this can be accomplished in two ways. Which method is applied can be selected as a configuration option. One of the methods is build using a conventional log-derivation approach for estimating the extinction profile, the other uses a new "local-

180 forward-modelling" approach. The two different approaches are described and discussed in Appendix A. The new approach generally produces "better behaved" extinction-to-backscatter ratio profiles. This is important since, in subsequent steps, the A-EBD algorithm will separate and classify layers using, in part, the extinction-to-backscatter ratio. S is also a primary input to the A-EBD algorithm. No multiple-scattering correction is performed at this stage, since that can only be done once an target classification has been performed (step 10).

185 In **step 10** the coarse layer structure calculated in step 5 is recalculated using the scattering ratios calculated in Step 4 as additional input to the layering algorithm. This re-recalculation (along with the subsequent Step) helps insure that sharp features present in the scattering ratios are captured. Then for each coarse layer, in **step 10** the each layer by itself is examined to see if the layer should be further subdivided. The basic idea is to test if it is valid to represent the layer as a homogeneous entity or if it is better to split the layer into a number of homogeneous sub-layers. The procedure relies on examining the behaviour of

190 a reduced chi-squared goodness-of-fit variable applied to the scattering–ratio, lidar–ratio and the depolarisation–ratio which is

7

calculated for all possible sub-layering for up to four distinct sub-layers. The layer splitting algorithm is described in Section 2.1.2 of Irbah et al. (2023).

Based on the fine layer structure calculated in Step 10, the mean backscatter, extinction, lidar–ratio and depolarization ratio are calculated. This information is then passed to the classification procedures (Steps 14 and 15) which are described in Sections 2.2 and 2.3 of (Irbah et al., 2023). It should be noted that extinction and backscatter information used at this stage have not been corrected for multiple-scattering effects, thus, the classification procedures are called using a version of the classification priors adjusted to approximately account for MS effects.

In **Step 17** the extinction and lidar-ratio values calculated in Step 9 are corrected for multiple-scattering effects. The treatment of multiple-scattering is treated in general within Section B and the specific adjustment of the values for extinction and backscatter within A-AER are treated within Appendix B4. The layers are then re-classified using a call to the A-TC procedures but this time using the classification priors appropriate for single-scattering. This can lead to situations where the classification changes compared to the results of the previous step. This is currently not checked for, but this option (and the option to iterate between Steps 14 and 17) could be implemented in the future (at the cost of more complexity and a slower processor run-time).

After steps 1 – 17 are completed for the whole frame, the data product file is written out including the layering and classification information.

2.3 A-EBD

After A-AER has been executed, the ATLID Extinction-backscatter and depolarization procedure is applied. The core of this procedure is built upon a column-by-column optimal estimation (OE) forward model inversion performed at a higher resolution than A-AER with the aim of supplying extinction and backscatter values for both 'weak' and 'strong' targets. A-EBD uses the classification and (where possible) the lidar-ratio estimates generated by A-AER as a starting point. Like all optimal-estimation approaches a *cost-function* (χ) is formulated which expresses the sum of the weighted difference between the observations and the observations predicted by a forward model ($\mathbf{F}$) given a certain state ($\mathbf{x}$) and the weighted difference between the state and and an a priori state ($\mathbf{x_a}$).

The particular cost function used by A-EBD can be written as

$$\chi^2 = [\mathbf{y} - \mathbf{F}(\mathbf{x})]^T \mathbf{S_e^{-1}} [\mathbf{y} - \mathbf{F}(\mathbf{x})] + [\mathbf{x_r^l} - \mathbf{x_a^l}] \mathbf{S_a^{-1}} [\mathbf{x_r^l} - \mathbf{x_a^l}], \tag{9}$$

where

- $\mathbf{y}$ is the observation vector including the observed Rayleigh and Mie attenuated backscatters

$$\mathbf{y} = \left(B_{R,1}^c, B_{R,2}^c, ... B_{R,n}^c, B_{M,1}^c, B_{M,2}^c, ... B_{M,n}^c \right)^T \tag{10}$$

where n is the number of range-gates, $B_{R,i}^c$ is the ratio of the observed Rayleigh attenuated backscatter corrected for the effects of molecular Rayleigh attenuation

$$B_{R,i}^c = b_R(z_i) \exp \left[2 \int_{z_{lid}}^{z_i} -2\alpha(z') dr(z') \right] \tag{11}$$

and $B_{M,i}^c$ is the ratio of the total Mie attenuated backscatter corrected for the effects of molecular Rayleigh attenuation i.e.

$$B_{M,i}^c = \left(b_{M,\parallel}(z_i) + b_{M,\perp}(z_i) \right) \exp \left[2 \int_{z_{lid}}^{z_i} -2\alpha(z') dr(z') \right] \tag{12}$$

- $\mathbf{x^l}$ is the logarithmic state-vector defined as:

$$\mathbf{x^l} = \log_{10}(\mathbf{x}) = \log_{10} \left(\alpha_{M,1}, \alpha_{M,2}, ... \alpha_{M,N}, S_1, S_2, .. S_{nl}, Ra_1, Ra_2, ... Ra_{nl}, C_{lid} \right)^T \tag{13}$$

where S are the lidar-ratios, R_a are the effective area radii, and C_{lid} is a factor used to account for calibration errors. Here N is the number of range-gates identified within A-AER as being **non-clear-sky** and nl is the number of layers for the along-track column being treated. This formulation (where the particulate extinction is set to zero for clear-sky range gates and the lidar-ratio and particle sizes are constant within layers) is used to reduce the dimensionality of the problem which can have a significant positive impact on the computational requirements. The log form is used to constrain the retrieved state-vector to be positive.

- $\mathbf{x_a^l}$ is the logarithmic a-priori state vector. Here defined as a vector consisting of the log base 10 values of the a priori lidar-ratios, effective area particle sizes and the value of C_{lid} appropriate for calibrated attenuated backscatter signals (i.e. 1) . Using a log form here is consistent with the a priori errors being proportional in nature rather than absolute.

$$\mathbf{x_a^l} = \log_{10}\left(\mathbf{x_a}\right) = \log_{10}\left(S_{a,1}, S_{a,2}, ..S_{a,nl}, Ra_{a,1}, Ra_{a,2}, ...Ra_{a,nl}, 1\right)^T \tag{14}$$

Note that here no a-priori constraints are placed upon the log extinction values so that they are not present in the a-priori state-vector. The a priori values of the lidar-ratio and and their associated error estimates are taken from the A-AER results, when quantitative retrievals are flagged as valid. Otherwise, The a priori values of the lidar-ratio and errors depend on the A-AER target classification. For the ice particle effective radii, the a priori values (and errors) are provided by the A-ICE procedure which is described in Section 2.3.2 or fixed values can be used (as specified in a configuration file). For water cloud and aerosols the effective radii are specified a priori by type.

- $\mathbf{S_a}$ is the a priori error covariance matrix. It is assumed that the a priori errors are uncorrelated so that the matrix takes a diagonal form. Here the form of the entries is the one appropriate for a logarithmic state-vector Kliewer et al. (2015) i.e

$$S_{a_{i,i}} = \log_{10}\left(1 + \sigma_{x_{a,i}}^2\right) \tag{15}$$

where $\sigma_{\mathbf{x_{a_i}}}$ is the a priori (linear)uncertainty assigned to the ith component of $\mathbf{x_a}$.

- $\mathbf{S_y}$ is the observational error covariance matrix. For practical reasons, in the present version of the algorithm, it is assumed that the errors are uncorrelated so that the matrix takes a diagonal form. In fact, the errors for the Mie and Rayleigh signals at the same altitudes will be correlated due to crosstalk. Here the form of the entries is the one appropriate for a logarithmic state-vector (Kliewer et al., 2015) i.e

$$S_{y_{i,i}} = \log_{10}\left(1 + \sigma_{y_i}^2\right) \tag{16}$$

where $\sigma_{\mathbf{x_{a_i}}}$ is the (linear)uncertainty assigned to the ith component of $\mathbf{Y}$.

- $\mathbf{F}$ is the forward model which predicts the Rayleigh and Mie attenuated backscatter profiles given the state-vector as an input. The forward-model accounts for multiple-scattering. The multiple-scattering lidar equation used in this work is described in detail in Appendix B and the exact discrete form used in this work along with its Jacobian is described in Appendix C.

2.3.1 A-EBD procedure

The optimal-estimation retrieval is embedded within a broader framework. A high-level flow diagram of the A-EBD component of the A-PRO processor is shown in Fig. 3. The **first Step** is similar to the first step of the A-AER procedure. That is, the L1 ATLID signal are re-binned to the JSG resolution and the auxiliary met data is read and processed etc. In addition, however, the A-AER results (layering structure, classification, retrieved extinction and lidar-ratios and error estimates etc.) are also read in.

The **2nd** step involves the set-up of the OE inversion. In particular:

– For the lidar-ratio elements of x_a and their associated error estimates, A-AER supplied values are used for layers when available.

– For layers where A-AER could not derive a valid quantitative lidar-ratio, a priori values based on the A-AER classification (e.g. ice-cloud, water cloud, aerosol(type)) are used.

– The per-layer effective area sizes and associated a priori uncertainties are based on the A-AER classification. For ice-clouds a temperature dependent parameterization can be used (see Section 2.3.2).

– The starting values for the extinction elements of the state-vector are taken from A-AER when valid. Otherwise they are based on either the layer-averaged scattering ratio and the a priori lidar-ratio when valid, or fixed values depending on the classification.

Once the OE problem has been set-up, within **step 3** the cost-function is minimized using a version of the well-known BFGS Quasi-Newton numerical minimization procedure (Press et al., 2007). The errors in the retrieved state-vector (**step 4**) are computed following the procedure outlined in Section 15.5 of Press et al. (2007).

Once all the columns have been processed, the A-TC procedure is called to assign a classification to each layer. The A-TC classification procedure is described in Sections 2.2 and 2.3 of (Irbah et al., 2023). In **step 6**, the "medium" and "low-" resolution fields are formed. Here, the extinction, backscatter and depolarization values are horizontally smoothed to "medium" and "low" resolutions. The smoothing is guided by the "weak-feature" mask (the complement of the "strong-feature mask", see Steps 2 and 7 of the A-AER procedure described in Section 2.2) modified to exclude E-EBD extinction values above an adjustable threshold, and excluding any water-cloud pixels. "Medium-resolution" is set to default to 40 km and "low-resolution" is set to a default of 150 km. These setting are adjustable and will be re-visited when ATLID in flight data is available. For pixels not covered by the "weak-feature" mask, the high resolution single JSG column values are used (i.e. merged with the low and medium fields respectively). Using the merged "low" and "medium" the A-TC classification routines are then called to generate the low and medium resolution classification fields (Step 7). Lastly, the A-ICE product variables are calculated (see Section 2.3.2.).

2.3.2 A-ICE

A-ICE is used to supply estimates of the ice-water-content (IWC) and effective particle radius using estimated extinction and the atmospheric temperature. One of two options can be specified. The two approaches used are based on (Heymsfield et al., 2005) and (Heymsfield et al., 2014b) respectively. The exact coefficients used in each approach are configurable and may be adjusted based on the experience with actual EarthCARE data. IWC and effective radii estimates are produced for all pixels identified as being ice in the A-TC product (Irbah et al., 2023).

3 Case Studies using Simulated Data

In this section, the application of A-PRO to the three main EarthCARE test scenes (Qu et al., 2023; Donovan et al., 2023) will

295 be presented and discussed. Here the focus is on the retrieved optical properties (extinction and lidar-ratio), however, target classification results (A-TC) are also presented. For each of the three scenes (Halifax, Baja, and Hawaii) overall results are presented, and a few extracts are presented in detail. More information is presented in Mason et al. (2023), where the results of various EarthCARE L2 retrieval algorithms are compared with each other and the model truth. It should be noted, however, that the data shown in this paper (Version 11) is not the same as the version used in (Mason et al., 2023) (V10). In general, the

300 results shown here (being based on a more developed version of A-PRO) are superior but not dramatically so.

One of the aims of this Section is to give the reader a "feeling" for the nature of the product that will be supplied to the community including the limitations and possible caveats. To this end, the sample retrievals have not been "overtuned" to produce optimal results. For example, it would be possible to tune the priors to the model scenes (e.g. lidar-ratios, F_{MSp}, Ra, η) to closely match the three scenes. This is not done here, since it is instructive to gain insight into the relative robustness of the

305 various retrieved variables in different circumstances given reasonable limited knowledge of the priors with respect to actual observations. For example, most of the ice clouds present in the test scenes have an associated lidar-ratio of 30 Sr, however, in these retrieval, an a priori value of 25 Sr with a relative uncertainty of 20% is used. The values of F_{MSp} are also fixed and were not tuned, these were set based on idealized off-line simulations (see e.g. Section B) which were conducted independently of the main tests scene scene construction process. As a result, bias differences from the model-truth are to be expected. These

310 differences will help guide investigations that will be conducted post-launch.

3.1 Halifax

The attenuated co-polar Mie, Rayleigh, and cross-polar backscatter signals as well as the corresponding A-FM Feature-mask (van Zadelhoff et al., 2023) for the Halifax scene are shown in Fig. 4. These fields, along with the X-JSG and X-MET products (Eisinger et al., 2023) form the inputs for A-PRO. The particle extinction products produced by A-PRO corresponding to the

315 inputs shown in Fig. 4 are shown in Fig. 5. The Black regions are regions flagged as being not valid (e.g. attenuated or otherwise invalid), the Black vertical "strip" is the result of "gap" in the simulated lidar signals after re-binning to the JSG. In Fig. 5, the differences between the different products can be seen. Compared to the A-EBD fields, the A-AER estimate is the smoothest, however, no extinction estimates flagged as being valid are generated for the "strong" e.g. clouds. For the A-EBD estimates it can be seen that the aerosol and thin ice cloud areas become smoother as the horizontal resolution decreases, however, the

320 cloud extinction regions are not smoothed (see the last step described in 2.3.1).

Two example regions of the Halifax scene extinctions results are presented in more detail within Fig. 6. In the profile plots of the retrieved extinction (α_r)the light-Blue regions correspond to the average estimated uncertainty in a relative sense i.e.

$$\frac{\overline{\alpha_r}}{1+\overline{\sigma}_{\alpha_r}} < \alpha_r < \overline{\alpha_r} + \overline{\sigma_{\alpha_r}}, \tag{17}$$

which is consistent with the logarithmic nature of the state-vector used in the retrievals. The Black-lines represent the estimate
error of the average profiles i.e.

$$\sigma_{\overline{\alpha_r}} = \frac{\sum_{i=1}^{N} \sigma_{i,\alpha_r}^2}{N^{1/2}}, \tag{18}$$

where N is the number of samples contibuting to the average.

The sample ice-cloud region (Bottom Left zoom) shows that in in this case, on the 10-km scale that the extinction values
above 10^{-2} km^{-1} are accurately retrieved (e.g. within a factor of 1.5), albeit with a low estimated precision. In the more
attenuated areas of the cloud at lower altitudes (e.g. below 8.75 km), the accuracy and precision degrade due to worse SNR
and the imperfect correction of MS effects. The 2nd region corresponds to a cloud-free aerosol case. Here it can bee seen that
on the 50 km^{-1} scale, for extinction values above 10^{-2} km^{-1} are retrieved with an accuracy of about 50 %.

The lidar-ratio retrievals corresponding to Figs. 5 and 6 are shown in Figs. 7 and 8 respectively. Here the fact that S is only
retrieved per-layer is evident (see esp. The Lower-Right panel of Fig. 8. In Fig. 7 it can be seen that the A-AER estimate, for
the cloud aerosol are generally too low (15-20 sr vs 25 for the model-truth) this is roughly consistent with may be expected due
to the limitations of correcting for multiple-scattering effects (see the discussion in Section B4). In the ABE optimal estimation
retrieval, the particle size is an element of the state-vector, and a fuller treatment of multiple-scattering is possible, thus EBD
generally retrieves lidar-ratios that are closer to the model truth. Referring to Fig. 8, it can be seen that the retrieved lidar-ratios
are within about 10-15% for the cirrus case. For the aerosol section presented in Fig. 8, (where multiple-scattering is less-
important) the retrieved lidar-ratios are generally within 10% and there is not such a greater difference between the AER and
EBD retrievals.

Within Figs. 7 and 8 it may be observed that the highest estimated values of the lidar-ratio occur in the aerosol layer at around
32.5 $^o N$. This is even clearer in Fig. 9 where it can be seen that the anomalously high estimated lidar-ratio leads to a miss-
classification of the aerosol type. This anomalous region coincides with the presence of a semi-transparent ice cloud present
above between about 8 and 10 km and is examined in more detail in Fig. 10. Referring to Section B, this is an example of the
decaying multiple-scattering tail beneath clouds influencing the signals below. The (g)–(k) sequence of panels show that the
Mie and Rayleigh attenuated backscatters are indeed "well-fitted" and the extinction is generally accurately retrieved (albeit
with large relative estimated uncertainty), however, the retrieved lidar-ratios exhibit large differences from the model-truth.
These errors are largely the result of the difficulty in fitting the decaying tail and the use of fixed-values for the f_{MSp} factors.
This observation, points to an avenue of inquiry once ATLID observations are available. In particular, if similar features in
actual ATLID retrievals are found below semi-transparent cloud layers, then it may be necessary to refine the setting to f_{MSp}
by e.g. including it the state-vector or parameterizing it as a function of multiple-scattering ratio and particle-size/type. The
(a)-(f) sequence of panels (the "Platt's approach" panels) are used to illustrate a related point. Namely, that not allowing for
the occurrence of tails in the foward model leads not only to higher lidar-ratio errors but much higher errors in the retrieved
extinction below the ice cloud.

3.2 Baja

The attenuated co-polar Mie, Rayleigh, and cross-polar backscatter signals as well as the corresponding A-FM Feature-mask (van Zadelhoff et al., 2023) for the Baja scene are shown in Fig. 11. The corresponding model-truth extinction, the retrieved low-resolution extinction field as well as details of two selected areas are shown in Fig. 12. The two sections selected here are

360   both cloud-free with no overlying semi-transparent cloud layers. The extinction are generally retrieved to within 10-15%. The corresponding lidar-ratio results are shown in Fig. 13. Here it can be seen that the lidar-ratios are retrieved usually within about 10-20 %.

A detailed view of an ice cloud region in shown in Fig. 14. Here it can be seen that, consistent to what was observed in general for the Halifax scene, that the extinction profile is well-retrieved (within 5-10%), however, the lidar-ratio is underestimated

365   (especially below 4 km). This is likely largely in part due to f_{MSp} not being set optimally. Even though below 4 km the ice cloud is giving way to optically thinner and smaller particle aerosol, the multiple-scattering ratio is still high (see Fig. 14), thus, it can be important to treat f_{MSp} accurately even if the target in question possesses a small effective radius and is not optically thick if underlies a layer which generates significant amount of multiple-forward-scattered light.

3.3 Hawaii

370   The attenuated co-polar Mie, Rayleigh, and cross-polar backscatter signals as well as the corresponding A-FM Feature-mask for the Hawaii scene are shown in Fig. 16. The corresponding model-truth extinction, the retrieved low-resolution extinction field as well as details of two selected areas are shown in Fig. 17. The extinction accuracy is seen to be consistent with the other two previously discussed scenes. Referring to the corresponding lidar-ratio details shown in Fig. 18 it can be seen that for the left selected area, that in this case, where the upper layer ice cloud is optically quite thin that it does not seen to much effect the

375   retrieval of underlying lidar-ratio. For the optically think ice-cloud selected area, the extinction profile is well-retrieved near up to the point of complete attenuation, however, as was seen before the retrieved lidar-ratio is biased low.
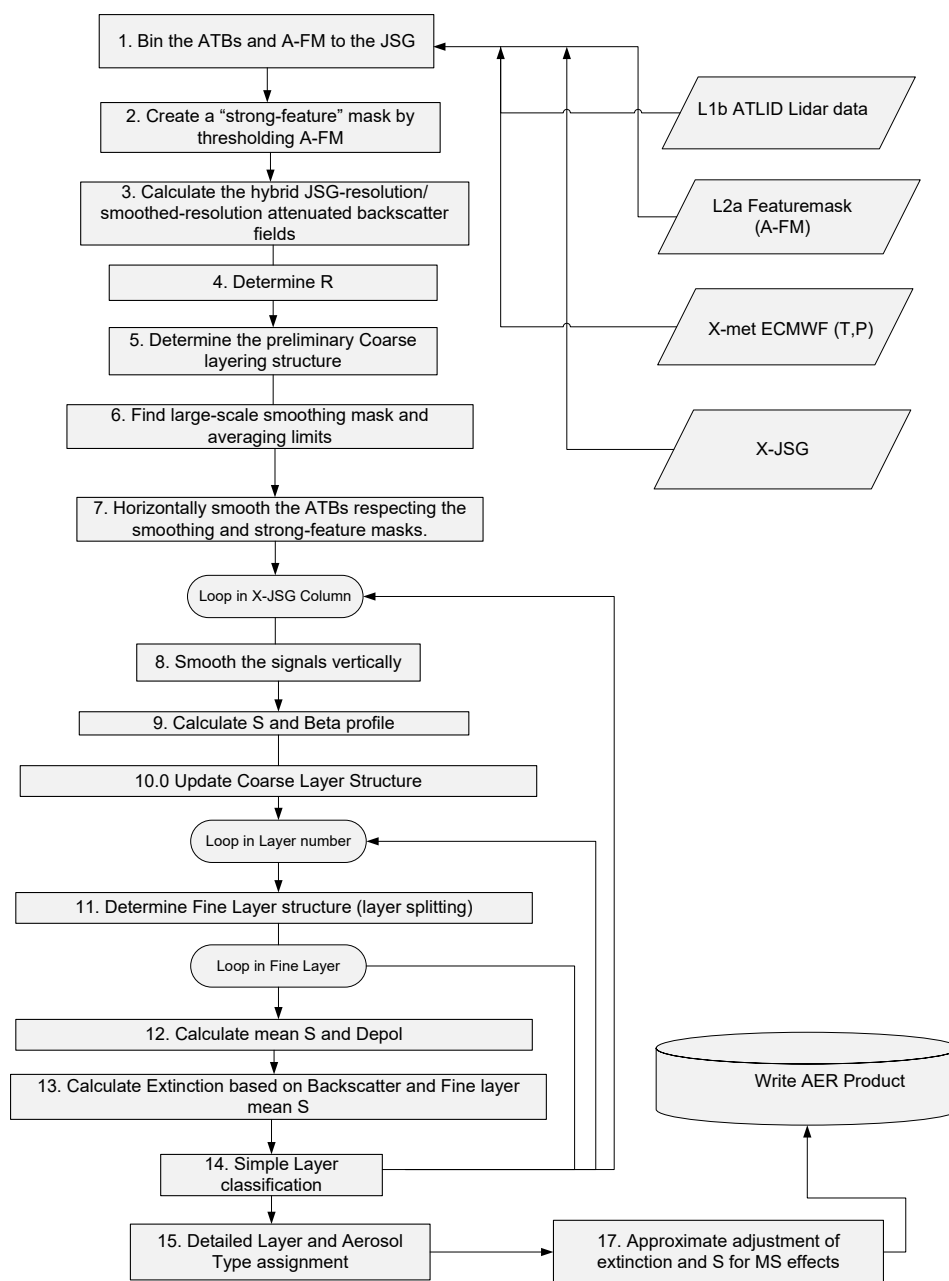
14

Figure 2. Schematic depiction of the structure of the A-AER component of the A-PRO processor.
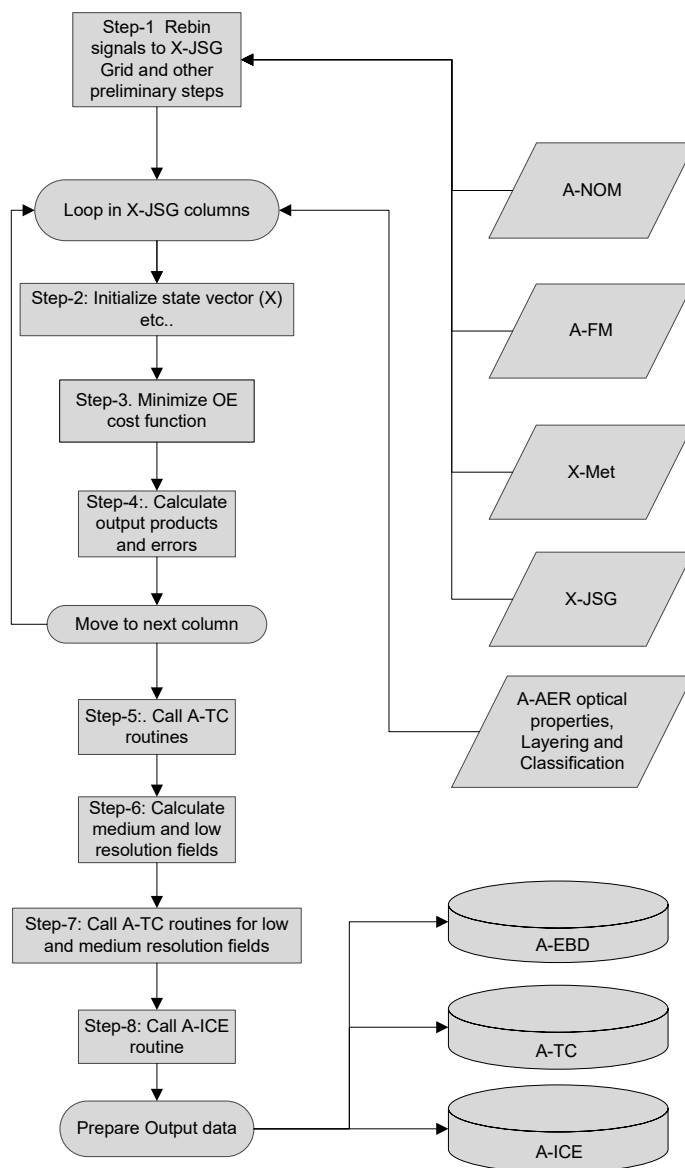
Figure 3. Schematic depiction of the structure of the A-EBD component of the A-PRO processor.
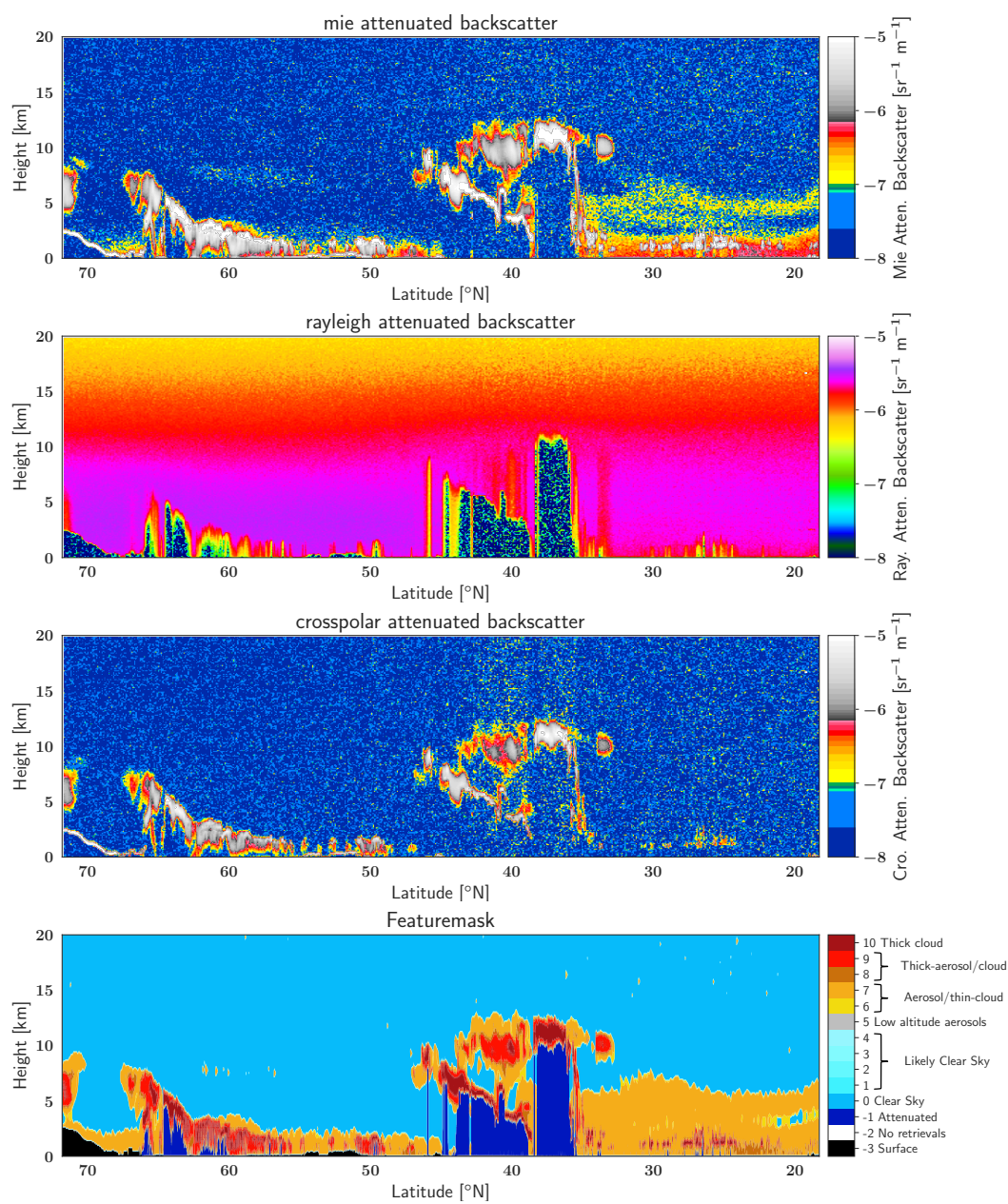
Figure 4. Simulated Mie, Rayleigh, and Cross-polar attenuated backscatter for the Halifax scene along with the A-FM L2 Featuremask.
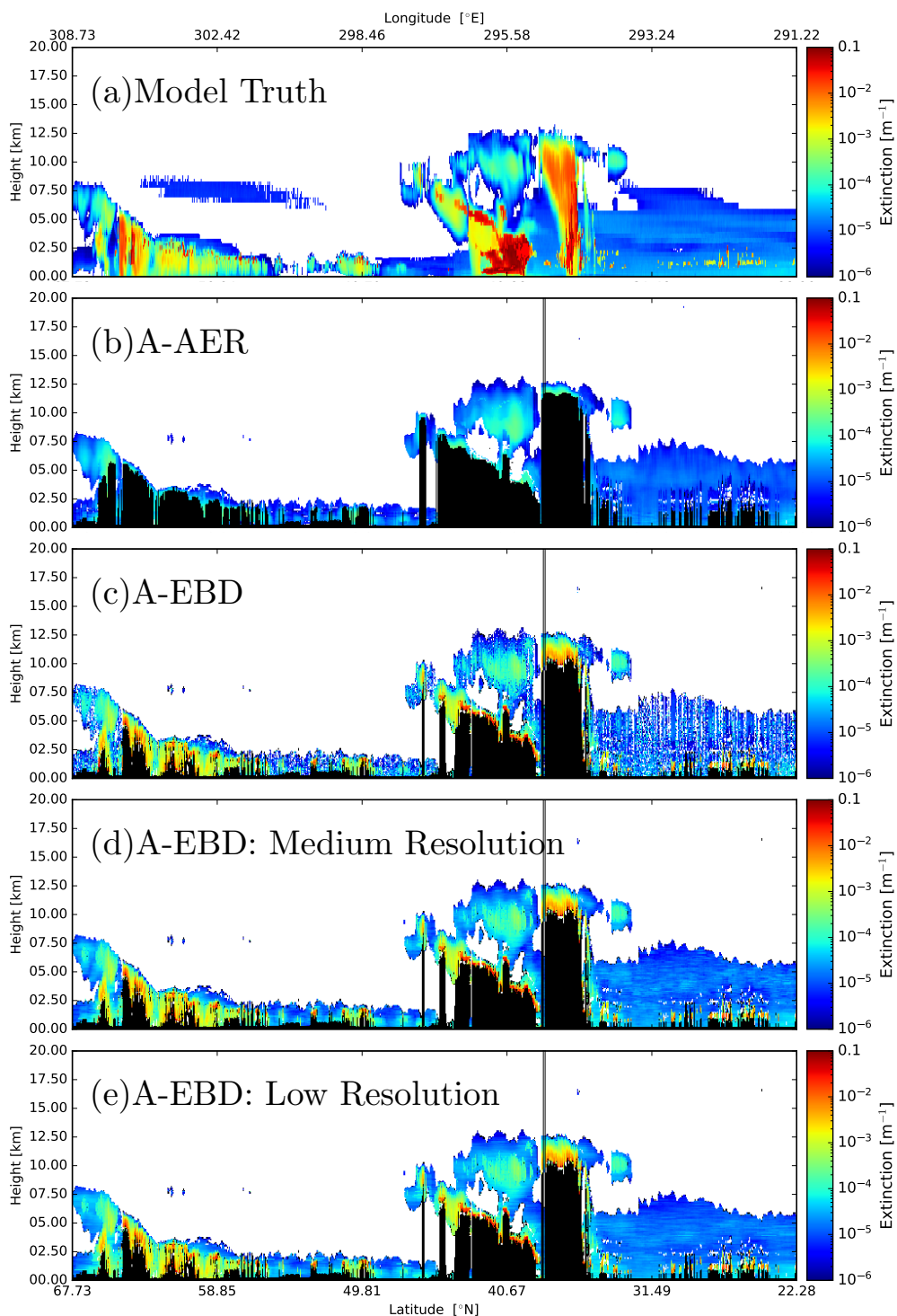
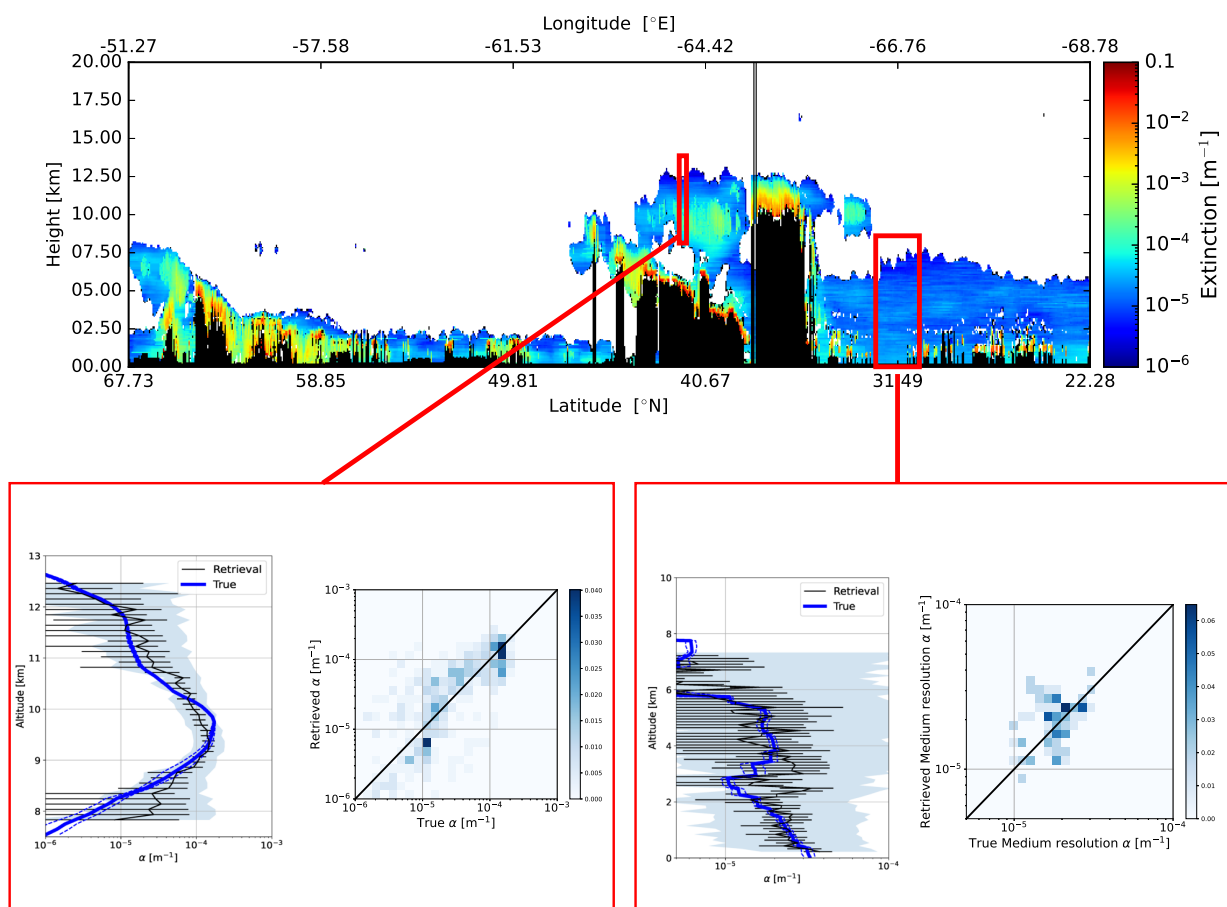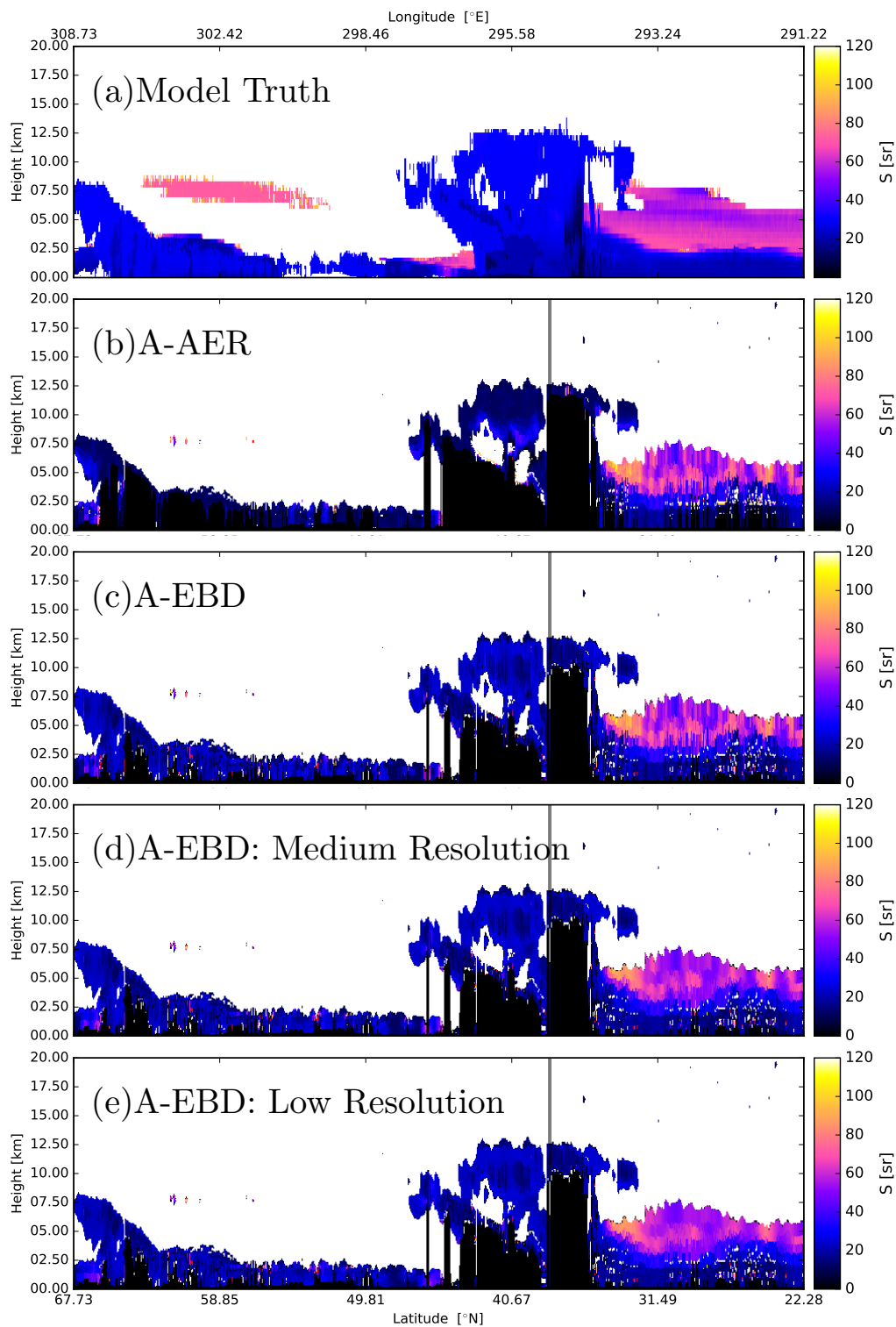**Figure 5.** Model-truth extinction for the Halifax scene and the corresponding A-AER and A-EBD products. Here "medium" resolution is 50 km while "Low" resolution corresponds to 100 km.

18

Figure 6. "Low-resolution" retrieved extinction for the Halifax scene (Top) and two representative average profiles. The Bottom-Left detail corresponds to a 10 km horizontal average of the A-EBD high-resolution extinction profiles and the corresponding model-truth extinction profiles. The Bottom-Right panel corresponds to a 50 km horizontal average. The Solid-Blue lines represent the average model-truth and the dashed-Blue lines delineate the +/- the model-truth standard deviation region. The solid-Black line represents the average retrieved extinction, the light-Blue shaded region the average relative uncertainty, and the error-bars represent the uncertainty of the mean retrieved profile The color-scale assigned to the True-vs-Retrieved histogram plots correspond to the normalized number of counts in each 2D histogram. The histograms were constructed using the medium resolution outputs in the respective windows and not the horizontally averaged data (which is displayed in the associated profile plots.)

Figure 7. Model-truth lidar-ratio for the Halifax scene and the corresponding A-AER and A-EBD products. Here "medium" resolution is 50 km while "Low" resolution corresponds to 100 km.
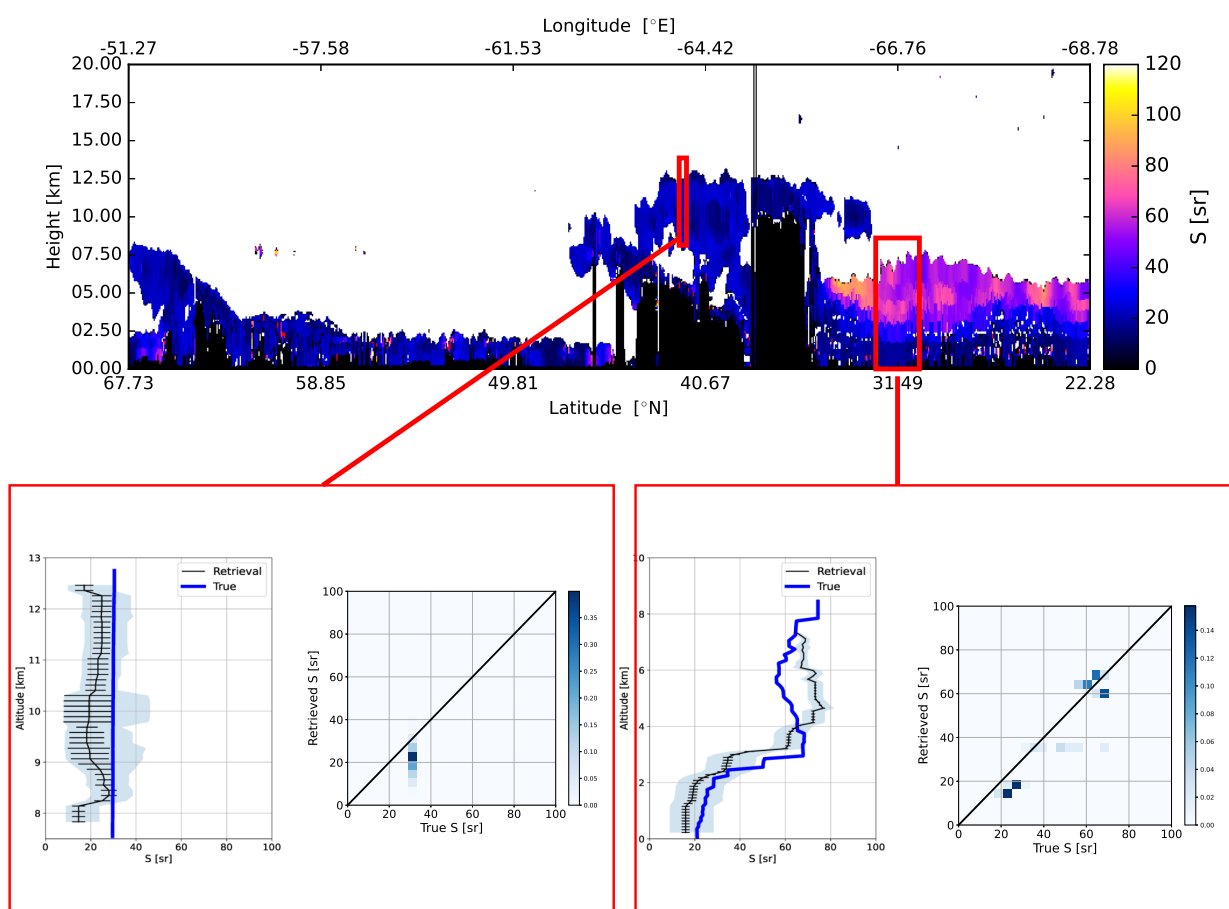
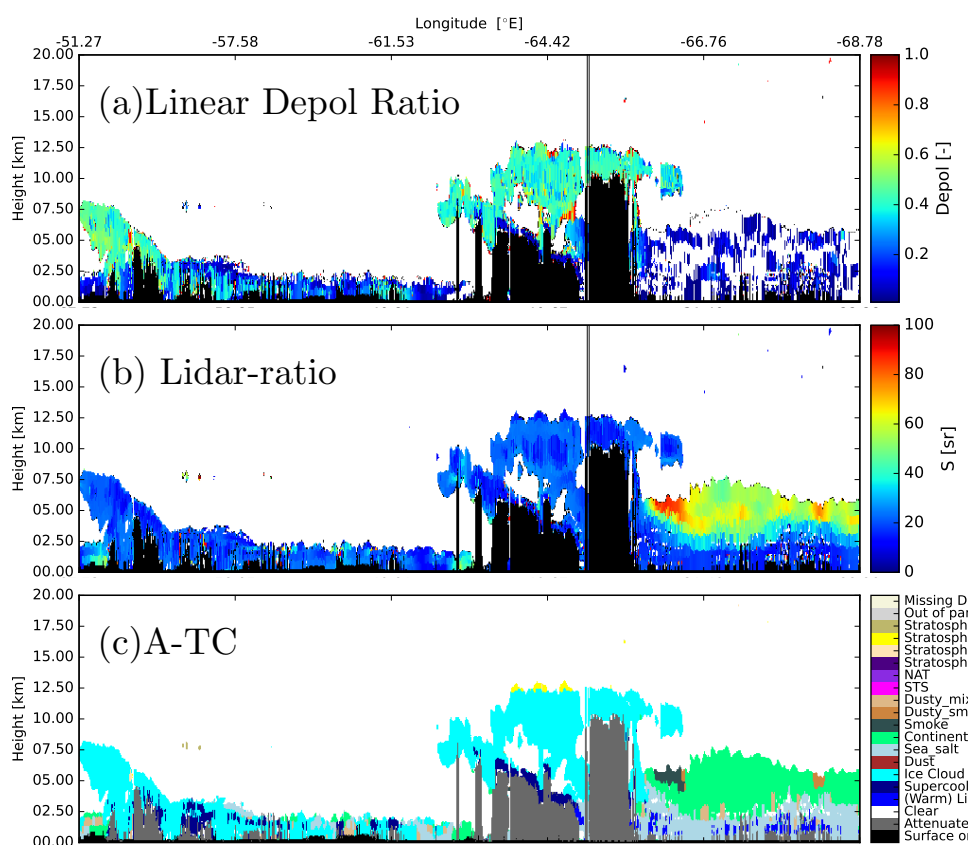**Figure 8.** As Fig. 6 except for the lidar-ratio.

Figure 9. (a) Low-resolution particulate depolarization ratio. (b): Retrieved low-resolution lidar-ratio and (c) the corresponding AC-TC classification field.
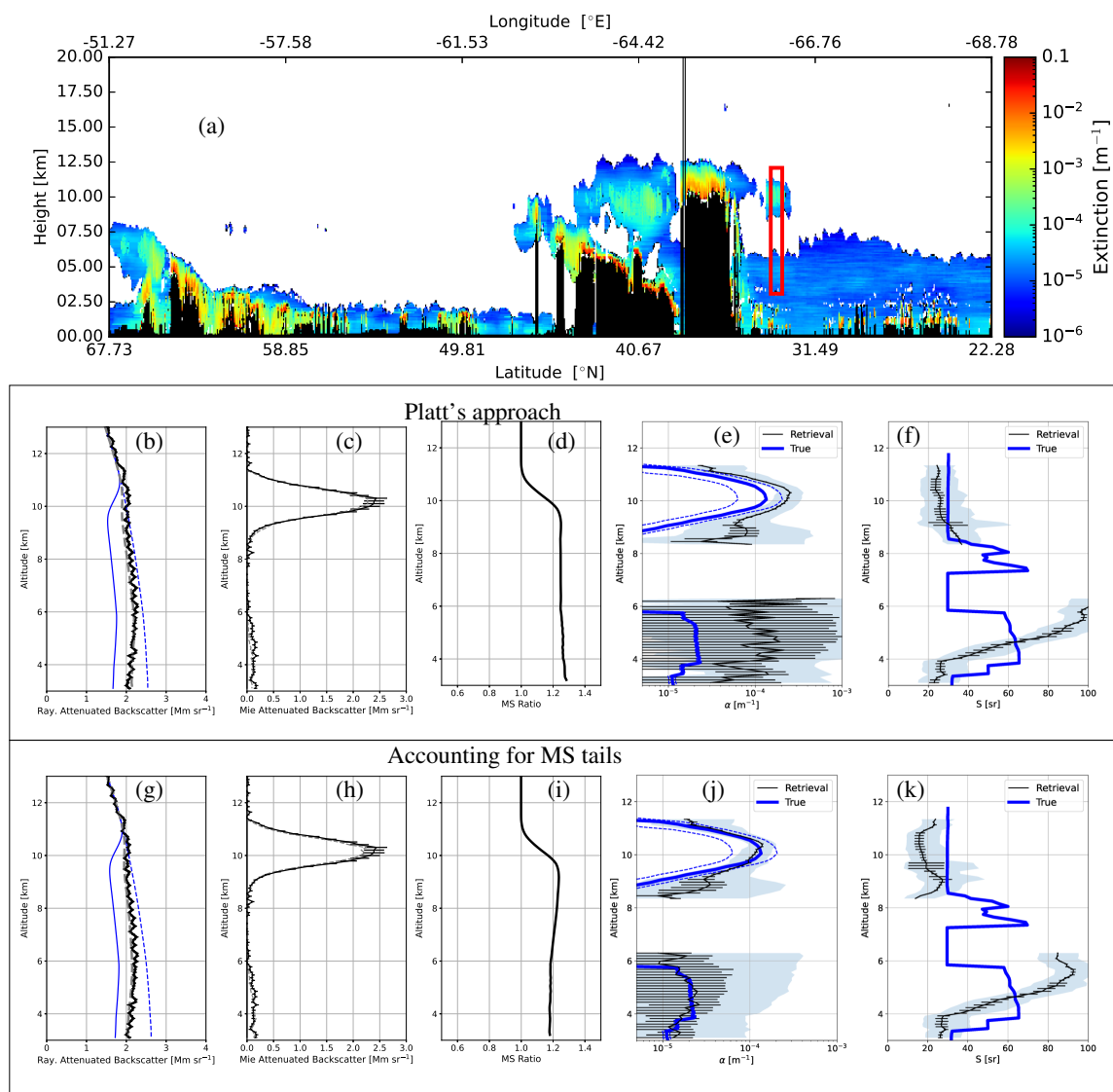
Figure 10. (a): Retrieved "low-resolution" extinction. (b): Average Rayleigh attenuated backscatter for the indicated (10km horizontal) interval (Black-line), the forward-model fit (Grey-dashed-line), the corresponding single-scatter Rayleigh attenuated backscatter (solid-Blue-line) and the Rayleigh-clear attenuated backscatter profile. (c): Average Mie attenuated backscatter for the indicated interval (Black-line) and corresponding forward-model fit (Grey-dashed-line). (d): Ratio of (total) multiple-scattering plus single scattering to single scatting return for the Rayleigh backscatter (e) Average retrieved extinction profile and associated standard deviation profile (Black-lines) and average model-truth extinction profiles (solid Blue-line) (f) Retrieved lidar-ratio corresponding to (e). The dashed blue-lines correspond to plus and minus the model truth standard deviation profile. The (b)–(f) plots correspond to retrievals conducting using Platt' approach while the (g)–(k) plots correspond to retrievals conducted using the default multiple-scatting (Platt+tails) model.
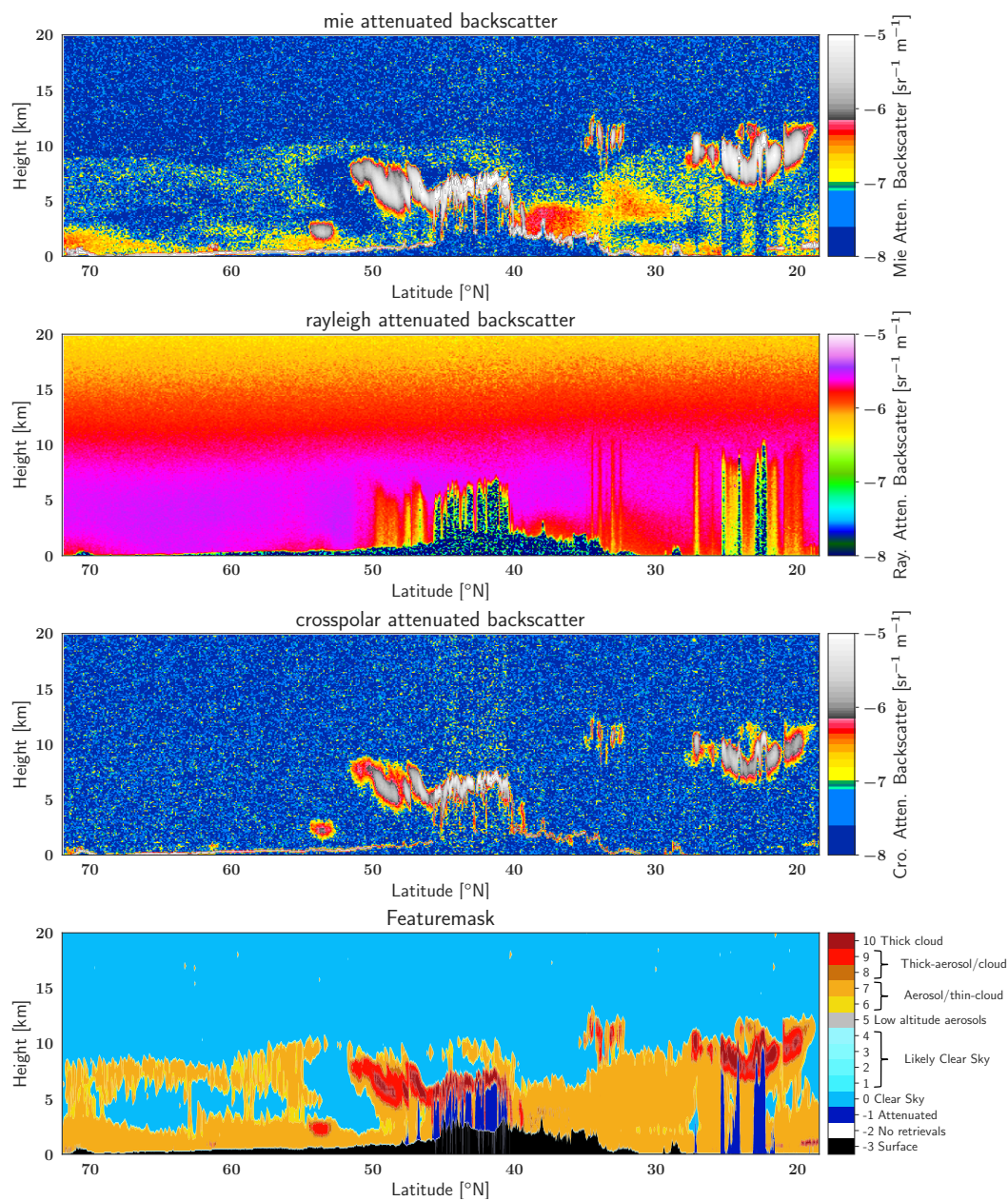
Figure 11. Simulated Mie,Rayleigh, and Cross-polar Attenuated back scatters for the Baja scene along with the corresponding A-FM L2 Featuremask.
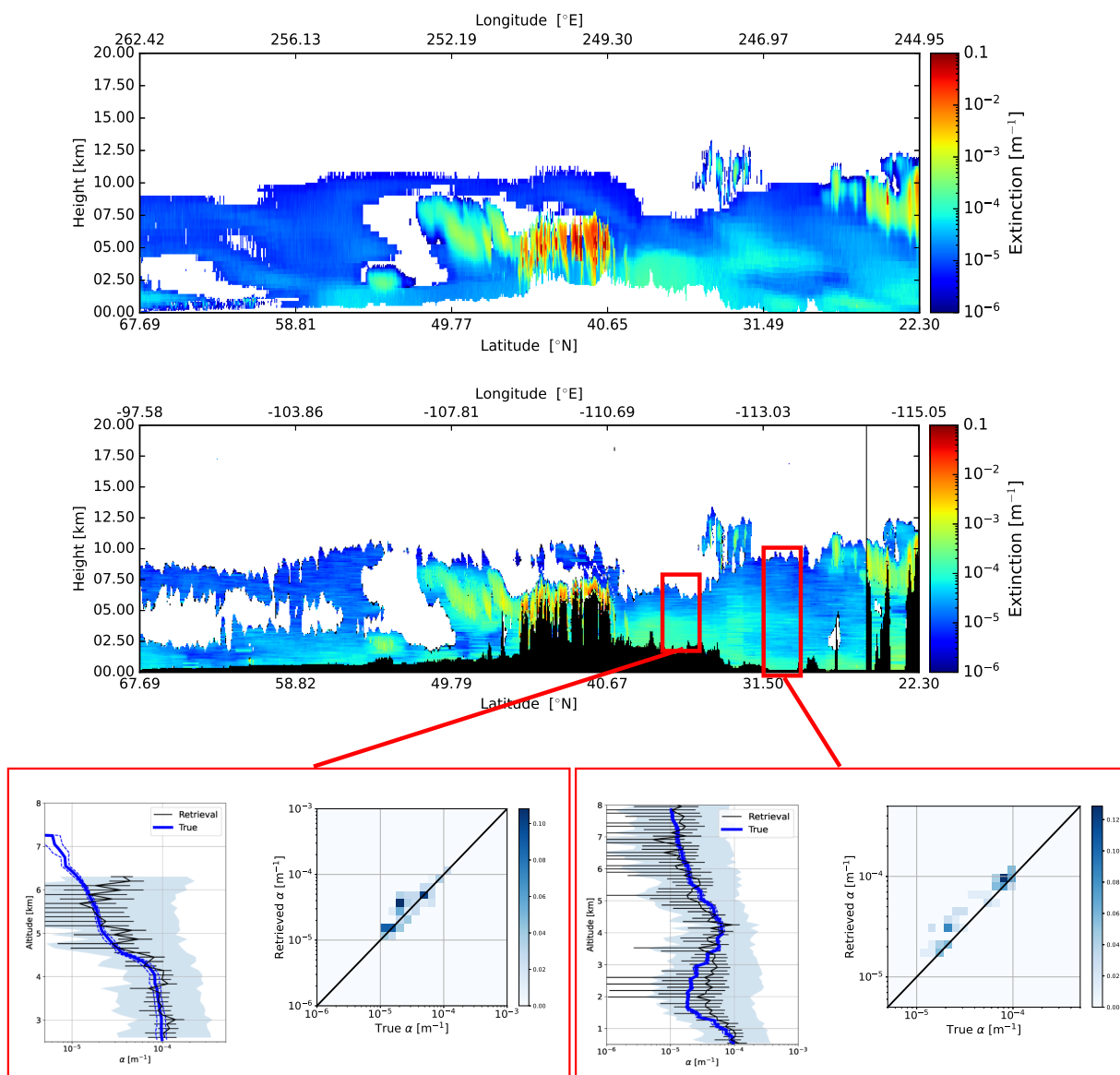
Figure 12. Model-true extinction (top-panel) and low-resolution retrieved extinction for the Baja scene (middle-panel) and two representative average retrieved profiles (bottom-panels) for the indicated intervals. The bottom panels correspond to the low-resolution (100km resolution)and the corresponding model-truth extinction profiles.
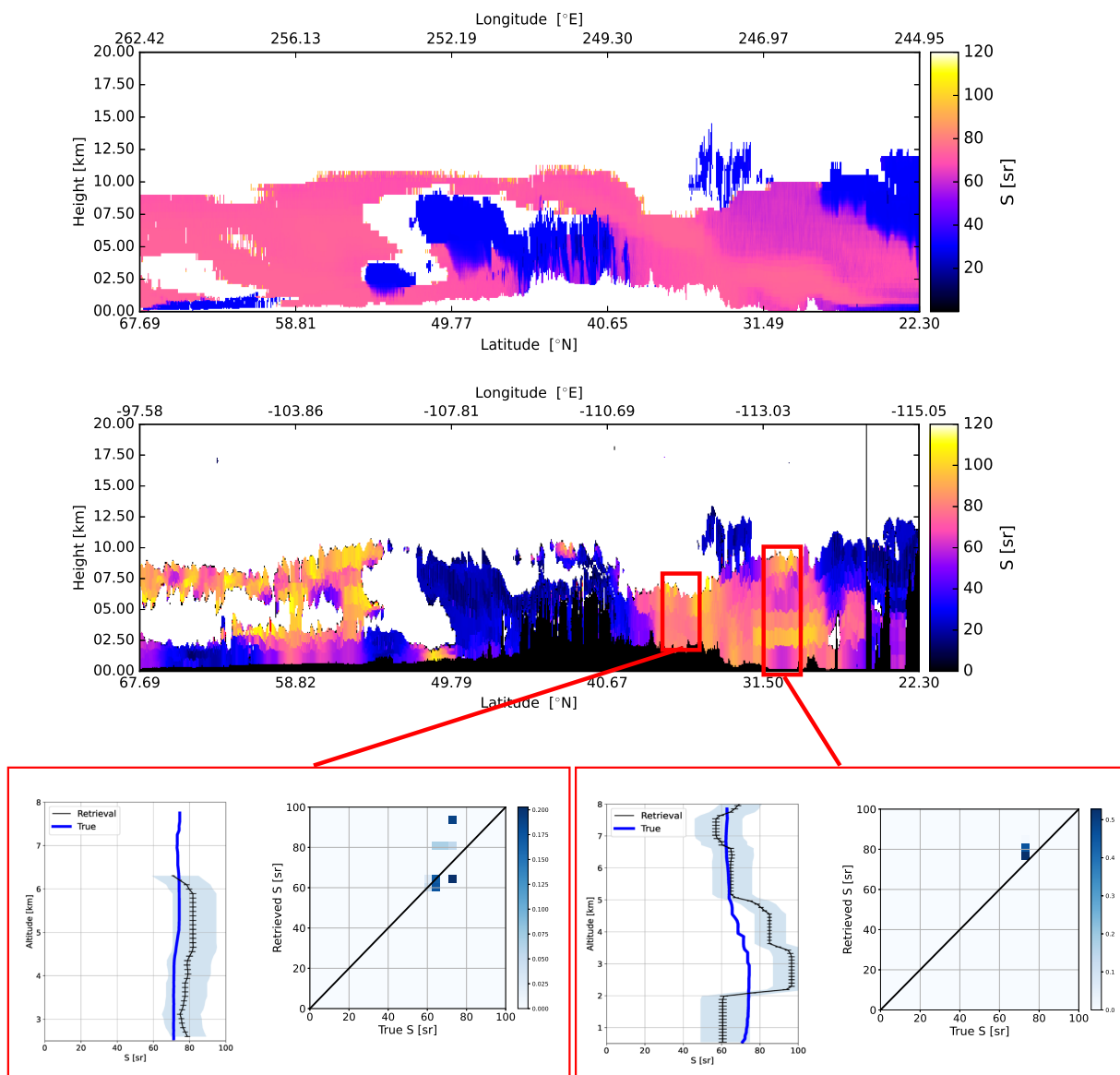
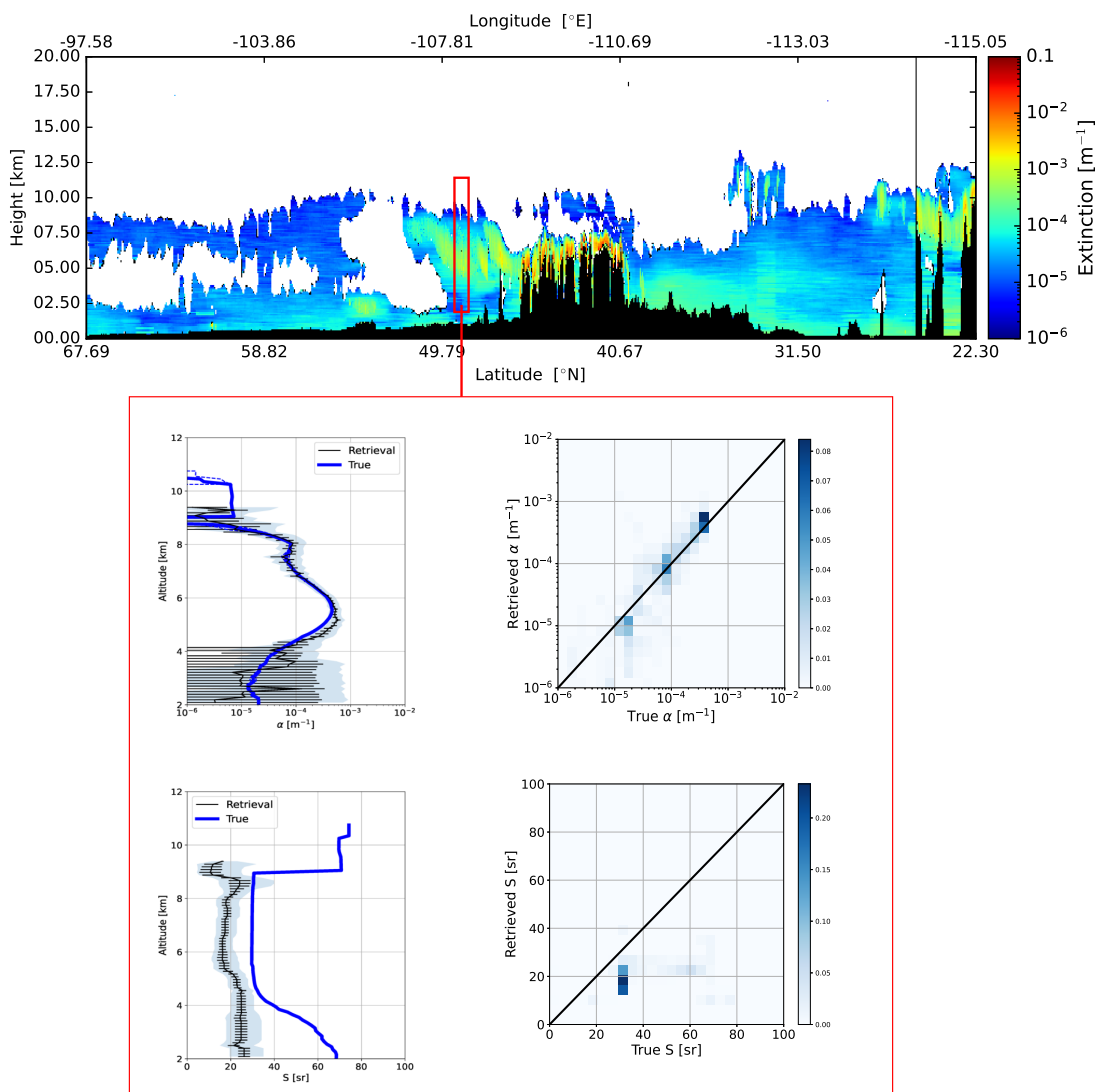**Figure 13.** As Fig. 12 except that lidar-ratio is considered.

Figure 14. Low-resolution retrieved extinction for the Baja scene (top-panel). The bottom panels correspond to the indicated 10km horizontal indicated region.
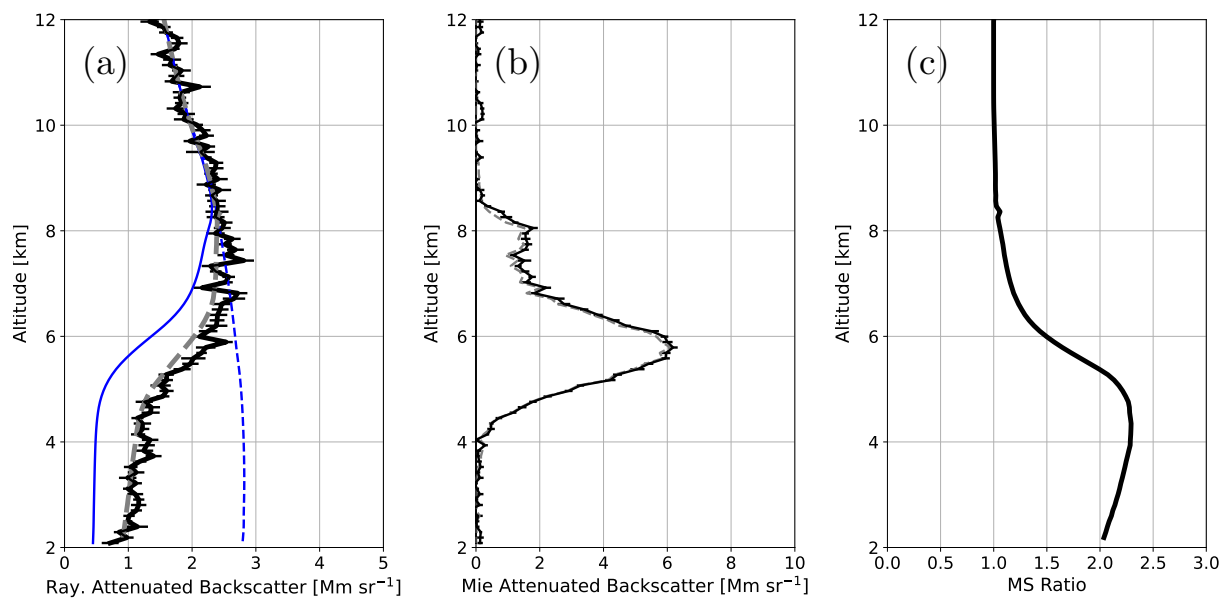
Figure 15. (a): Average Rayleigh attenuated backscatter for the interval indicated in Fig 14 (Black-line), the forward-model fit (Grey-dashed-line), the corresponding single-scatter Rayleigh attenuated backscatter (solid-Blue-line) and the Rayleigh-clear attenuated backscatter profile. (b): Average Mie attenuated backscatter for the indicated interval (Black-line) and corresponding forward-model fit (Grey-dashed-line). (c): Ratio of (total) multiple-scattering plus single scattering to single scatting return for the Rayleigh backscatter.
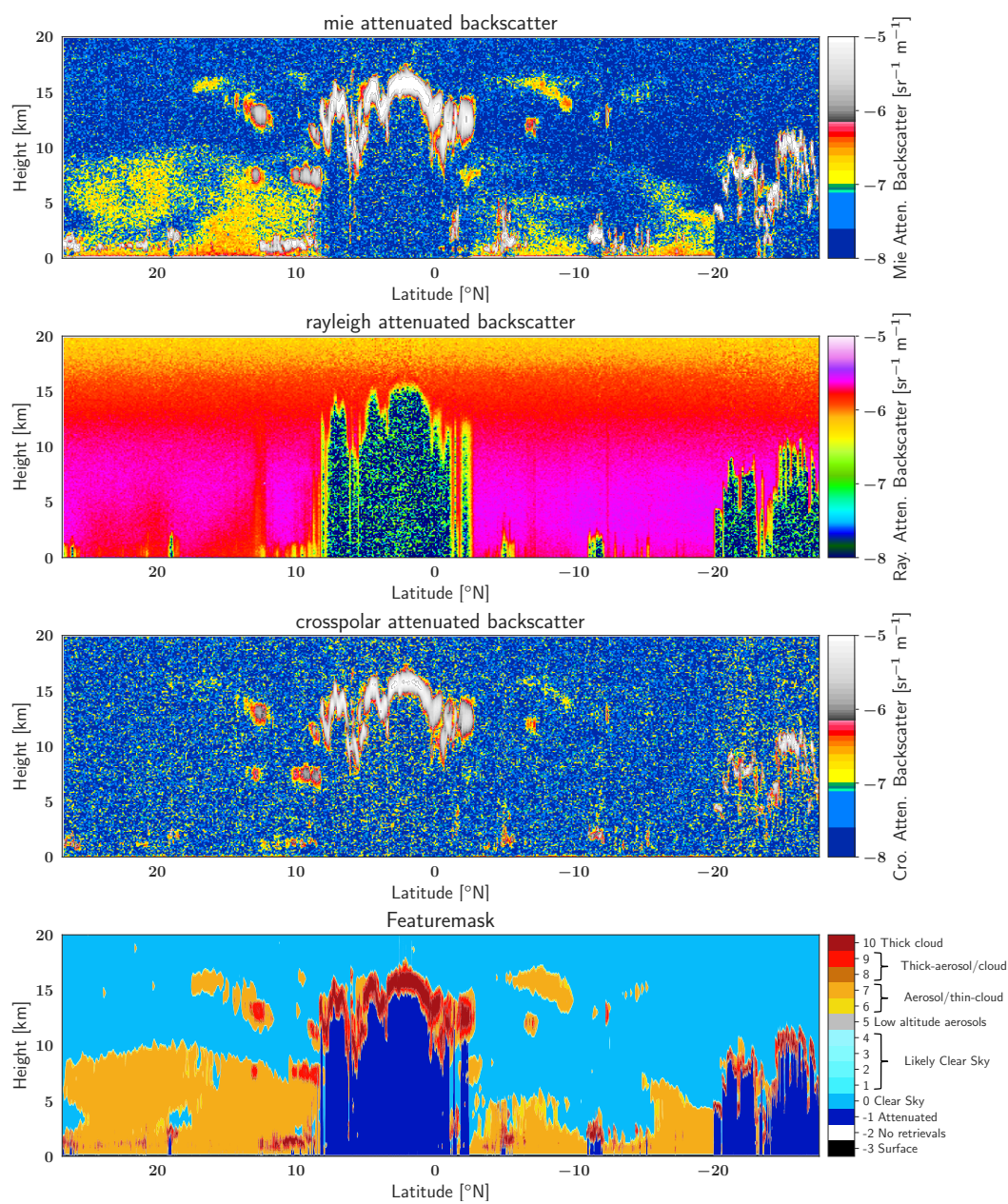
Figure 16. Simulated Mie,Rayleigh, and Cross-polar attenuated back scatters for the Hawaii scene along with the A-FM L2 Featuremask.
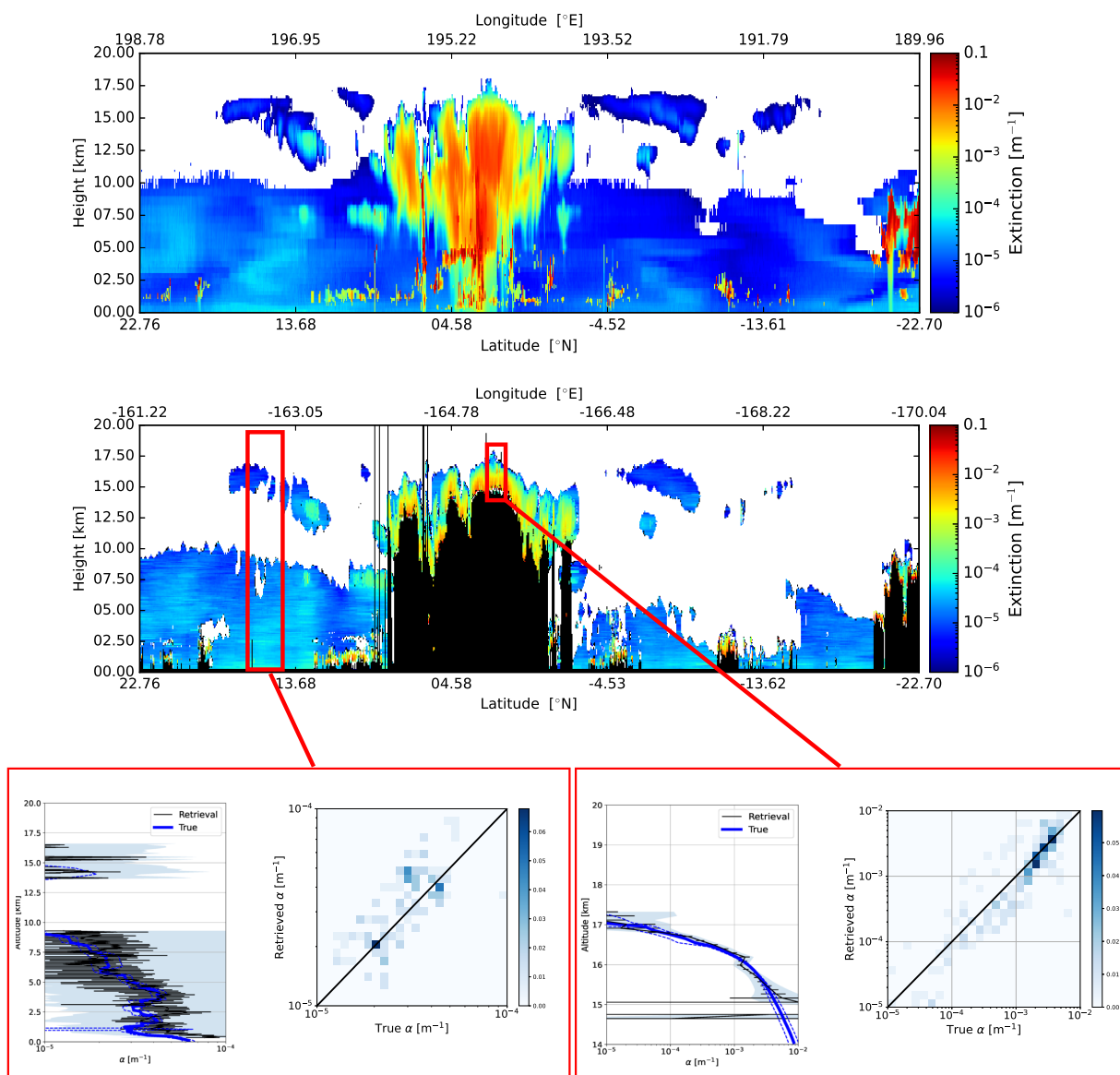
Figure 17. Model-true extinction (top-panel) and low-resolution retrieved extinction for the Hawaii scene (middle-panel) and two representative average retrieved profiles (bottom-panels) for the indicated intervals. The bottom-Right panels correspond to the low-resolution (100km resolution) and the corresponding model-truth extinction profiles while the bottom-Left corresponds to a 10 km horizontal interval.
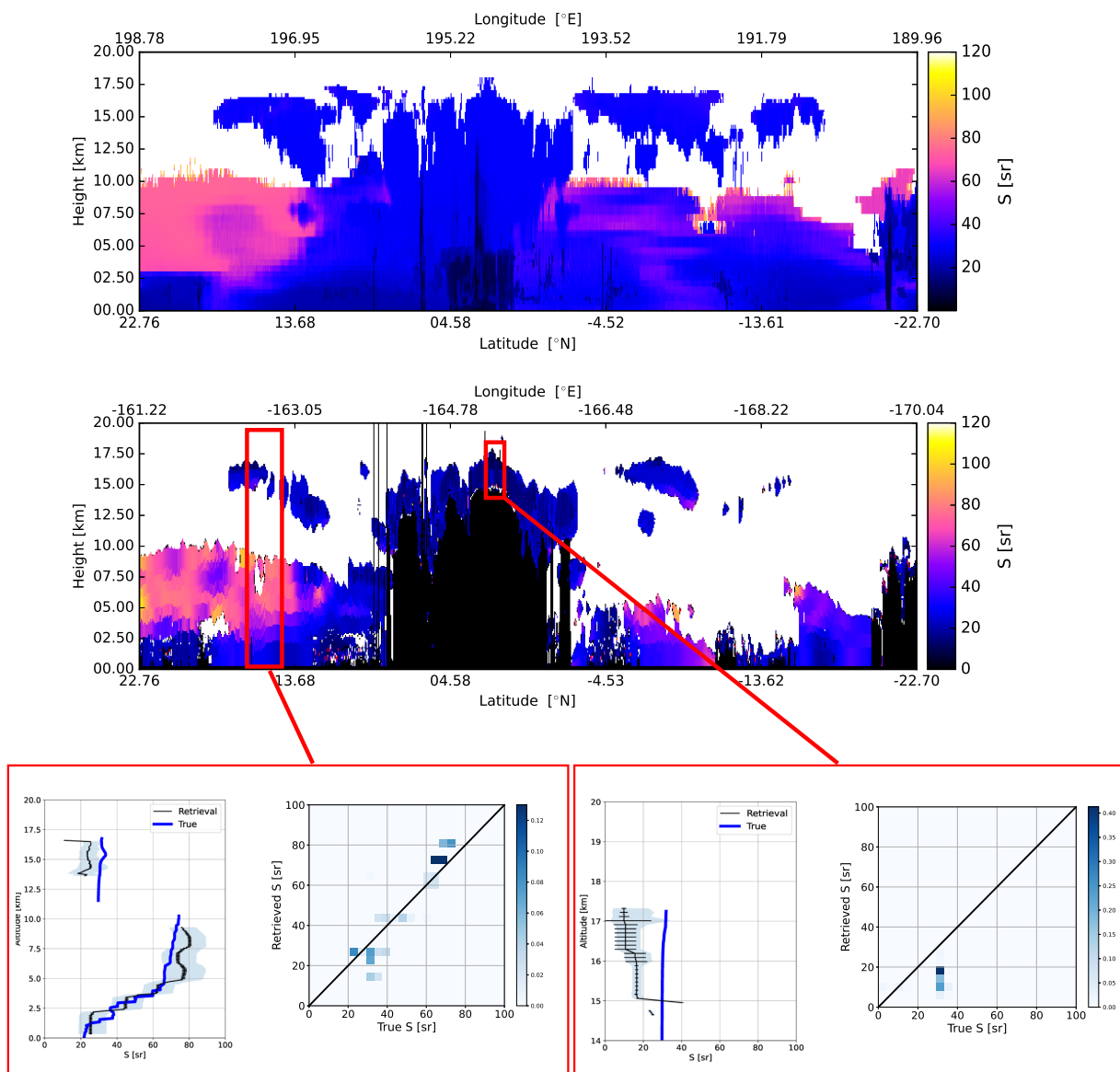
Figure 18. As Fig. 17 except that lidar-ratio is considered.

4 Conclusion and Outlook

The accurate retrieval of aerosol and cloud properties from space-based lidar is a challenging endeavor, even when the extra information provided by an HSRL system is exploited. The generally low SNR ratios involved coupled with the need to respect
380 the structure of the aerosol and cloud fields being sensed are particular challenges. A-PRO addresses these challenges by implementing a multi-scale approach resulting in a viable practical approach for both clouds and aerosols.

In this paper, a detailed overview of the A-PRO processor has been presented as well. The focus has been purposely limited to the extinction and lida-ratio retrievals. For a more complete picture, the interested reader should also consult Irbah et al. (2023) where the layer determination and classification procedures are detailed.

385 The development of the A-PRO processor has mainly been based on synthetic data (though a "cousin" algorithm called AEL-PRO has been applied to Aeolus (Straume, A.G. et al., 2020) data which will be the subject of another paper) and, no doubt, further refinements and extensions will be made when actual ATLID observations are available. One of the issues that has been noted, and indeed highlighted within this paper, is the potential difficulty in properly accounting for multiple-scattering effects. Retrievals below higher scattering layers can be affected by the presence of "tails" which can be difficult to accurately
390 model. Further, it is likely that a more comprehensive investigation and treatment of the role of anisotropic backscattering of multiple-scattered light (i.e. issues surrounding the f_{Msp} factor. It seems that often, in situations where multiple-scattering is important, that the extinction is more robustly retrieved than the lidar ratio. This is not surprising given that the extinction information is closely related to the Rayleigh signal profile which can be modeled, independently of f_{Msp}. The modeling of the Mie backscatter signal involves both S and f_{Msp}, this extra degree of freedom can create additional uncertainty when
395 retrieving the backscatter (or equivalently the lidar-ratio). Based upon further simulation-based studies as well as actual ATLID observations, this issue will be revisited and may results in extensions to the A-PRO procedures (i.e. paraeterization of f_{Msp} or including f_{Msp} in the state-vector of the A-EBD optimal-estimation algorithm).

who unexpectedly passed away recently. Tobias was eagerly looking forward to EarthCARE's launch, a mission to which he had dedicated a considerable span of his career. His support for the science community, collaborative approach and enthusiasm for the mission science will not be forgotten.

Competing interests. The authors declare that they have no conflict of interest.

410 **Appendix A: A-AER extinction, backscatter and lidar-ratios retrieval methods**

A0.1 Standard Estimation of lidar-ratio, extinction, and backscatter

Neglecting multiple-scattering effects for the time being and using Eqns. 8–6 we define

$$B_{M,hv} = F_{hv}\left(\beta_M \exp[-2\tau_M]\right) \tag{A1}$$

and

415 $$B_{R,hv}^{Rat} = F_{hv}\left(\exp[-2\tau_M]\right) \tag{A2}$$

Taking the range derivative of Eq. A2 and re-arranging yields an expression for the particulate extinction i.e.

$$\alpha_M(r) = -\frac{1}{2}\frac{dB_{R,hv}^{Rat}}{dr}\frac{1}{B_{R,hv}^{Rat}}, \tag{A3}$$

and dividing Eq. A2 by Eq. A1 yields an expression for the particulate backscatter coefficient i.e.

$$\beta_M(r) = \frac{B_{M,hv}}{B_{R,hv}^{Rat}}. \tag{A4}$$

420 Dividing the two previous equations then yields an expression for S i.e.

$$S(r) = -\frac{1}{2}\frac{dB_{R,hv}^{Rat}}{dr}\frac{1}{B_{M,hv}}. \tag{A5}$$

Deriving the extinction, backscatter and the associated lidar extinction-to-backscatter ratio using any approach related to that just outlined in which the signals are "smoothed" either explicitly or implicitly can lead to inaccurate results for the determination of S e.g. near the edges of clouds or aerosol regions. This is due to fact that the extinction information (which is 425 related to the signal derivative) and the backscatter information are linked to different vertical scales. In particular, the vertical derivative of the ATBs can not be unambiguously be linked to a single range-bin but can only be assess using two or more bins, however, the backscatter can be assessed, in principle at the scale of a single range-bin. This fundamental difference in the scale at which the extinction and backscatter information can be retrieved gives rise to undesirable edge effects. This problem can be made worse when vertical smoothing of the ATBs over a number of range-gates must be applied in order to increase

430 the effective SNR as is done here. In effect, applying the same smoothing strategy to both the Rayleigh and Mie ATBs, due to their dissimilar structure, does not result in the S-ratio being preserved even in cases where no noise were to present.

One of the uses of the S profiles within the A-AER is to help determine the layer-structure (See steps 10–11 in Section 2.2) and spurious features in the S profile can give rise to spurious layers. In part for this reason, an alternation procedure was developed and implemented which tends to produce fewer edge effects in the S determination process. This procedure is

435 described subsequently.

A0.2 Local Forward-modeling based estimation of S, extinction and backscatter

An approach which attempts limit the issues involved with spurious edge effects with S profile determinations is to perform a local forward model fit which, in a sense, puts the retrieved extinction and backscatter on the same scale. The basic idea is to use find the best value of S over a vertical fitting window which together with the conventionally derived backscatter profile

440 best predicts the observed Mie and Rayleigh ATB profiles.

As a starting point, the backscatter profile and extinction profiles and the subsequent values of S are determined using Eq. A4. Then the algorithm proceeds as follows.

1. For the fitting window the average backscatter is determined

$$\overline{\beta_M} = \frac{\sum_{i=i_{bot}}^{i_{top}} \beta_{M,i}}{N} \tag{A6}$$

445 i_{top} and i_{bot} are the range indices of the fitting window boundaries and N is the number of range-gates in the fitting window.

2. Using a specified value of S, the average particulate extinction within the fitting window $\overline{\alpha_M}$ is estimated i.e.

$$\overline{\alpha_M} = S\overline{\beta_M} \tag{A7}$$

450 3. The un-normalized predicted local profiles corresponding to $B_{R,hv}^{Rat}$ and $B_{M,hv}$ are calculated as:

$$B_{R,hv,i}^{'Rat} = \exp[-2\tau_{M,i}] \tag{A8}$$

and

$$B_{M,hv,i}^{'} = \overline{\beta_M}\exp[-2\tau_{M,i}] \tag{A9}$$

where $\tau_{M,i} = \alpha_M(r_i - r_o)$, where r_o is the value of the range gate closest to the lidar within the fitting window and r_i is

455 the range of the ith range-gate within the fitting window.

4. The local calibration factor (C_{loc}) which normalizes the profiles calculated in the previous step with respect to the observations is calculated i.e

$$C_{loc} = \frac{\sum \left(B_{M,hv,i} + B_{R,hv,i}^{Rat} \right)}{\sum \left(B_{M,hv,i}' + B_{R,hv,i}'^{Rat} \right)} \tag{A10}$$

where the summation is carried out over the fitting window.

5. The Chi-sq difference between the local forward–modelled and the corresponding observations is calculated as well as its derivative with-respect to S i.e.

$$\chi^2 = \sum \left(\frac{B_{M,hv,i} - C_{loc}B_{M,hv,i}'}{\sigma_{B_{M,hv,i}}} \right)^2 + \sum \left(\frac{B_{R,hv,i}^{Rat} - C_{loc}B_{M,hv,i}'^{Rat}}{\sigma_{B_{R,hv,i}^{Rat}}} \right)^2 \tag{A11}$$

and

$$\begin{aligned}
\frac{d\chi^2}{dS} = {} & 2\sum \left(\frac{C_{loc}B_{M,hv,i}' - B_{M,hv,i}}{\sigma_{B_{M,hv,i}}^2} \right) \overline{\beta_M} \left(-2C_{loc}\exp[-2\tau_{M,i}]\frac{d\tau_{M,i}}{dS} + \exp[-2\tau_{M,i}]\frac{dC_{loc}}{dS} \right) \\
& + 2\sum \left(\frac{C_{loc}B_{R,hv,i}'^{Rat} - B_{R,hv,i}^{Rat}}{\sigma_{B_{R,hv,i}^{Rat}}^2} \right) \left(-2C_{loc}\exp[-2\tau_{M,i}]\frac{d\tau_{M,i}}{dS} + \exp[-2\tau_{M,i}]\frac{dC_{loc}}{dS} \right)
\end{aligned} \tag{A12}$$

where,

$$\frac{d\tau_{M,i}}{dS} = \frac{\tau_{M,i}}{S} \tag{A13}$$

and

$$\frac{dC_{loc}}{dS} = 2\frac{\sum \left(B_{M,hv,i} + B_{R,hv,i}^{Rat} \right)}{\left(\sum B_{M,hv,i}' + B_{R,hv,i}'^{Rat} \right)^2} \sum \left(\overline{\beta_M} + 1 \right) \exp[-2\tau_{M,i}]\frac{d\tau_{M,i}}{dS} \tag{A14}$$

Here, the error estimates (the σ term) are calculated using standard-error propagation techniques based on the estimated random error in the observed Rayleigh and Mie attenuated backscatters.

6. The value of S that minimizes χ^2 is found numerically using the Secant method applied to $\frac{d\chi^2}{dS}$. For the initial iteration, the values of S generated by the application of Eq. (A4) are used. The Secant iteration continues (looping back to step 5.) until a maximum number of iterating is reached (usually set to 10) or successive value of S are within a set tolerance (e.g. 1%).

7. The uncertainty in the retrieved value of S is estimated according using a scaled Chi-sq approach i.e.

$$\sigma_S = \sqrt{2\left(\frac{d^2\chi^2}{dS^2} \right)^{-1}} \sqrt{\frac{\chi_{Min}^2}{i_{top} - i_{bot} - 2}} \tag{A15}$$

where χ_{Min}^2 is the minimum value of the cost-function obtained in the previous step.

8. Using the backscatter profile and S the extinction profile is determined along with its associated uncertainty.

The procedure described above is numerically based, but it is fast and does have an advantage compared to more conventional methods, in particular the S retrievals are better behaved near the edges of scattering layers. This is illustrated in Fig.A1 where the results of an simple idealized simulation are presented. Here, a simple two–layer aerosol field was used to simulate Rayleigh and Mie attenuated backscatter profiles. Panel B shows the noiseless ATB signals both at the native ATLID resolution of 100m and at a retrieval resolution of 300 m, it is clear that the smoothing affects the Mie ATB signals more than the corresponding Rayleigh profile. This is further reflected by the large oscillation in the extinction-to-backscatter retrieved using the conventional approach. The local-forward-modelling approach though yields generally superior results near the layer boundaries.

Appendix B: Treatment of multiple-scattering for ATLID in A-PRO

The inversion of ATLID lidar signals requires a fast, yet accurate treatment of lidar multiple scattering. Example simulated signal profiles for an idealized cirrus cloud are shown in Fig. **?**. Here three different models of different complexity have been applied, namely Monte-Carlo (MC), the reduced extinction approach due to Platt (Platt, 1981), and the quasi-small-angle (QSA) approach of Hogan (Hogan, 2008; Hogan and Battaglia, 2008). The Monte-Carlo results were calculated using the ECSIM lidar radiative transfer model (Donovan et al., 2015) and are, here, considered the most accurate. Here it can be seen that the QSA results are close to the MC results both within and below the cloud. Platt's approach performs well within the confines of the cloud but can not follow the shape of the "tails" arising from the decay of the signal towards single-scattering levels below the cloud base.

Hogan's approach is accurate and orders of magnitude faster than MC calculations. However, it is still much slower than the corresponding single-scattering case. Platt's approach on the other hand, is as fast as calculating the single-scattering return. In this work, a novel approach is developed which, in terms of complexity and speed, is between the approaches due to Platt and Hogan respectively.

We first discuss Platt's effective extinction approach and discuss how this can be extended to handle the phenomenon of decaying "tails".

B1 Platt's approach

Within Fig. B1, it can be noted that, within the cloud, that the observed signal closely resembles a less attenuated version of the single-scattering signal. This is to be expected when the particles are large compared to the wavelength of the laser light so that half the scattered energy is scattered forward in a narrow diffraction lobe and largely stays within the lidar receiver file-of-view. This result was noted by Platt (1976) and forms the basis of a simple method for accounting for Multiple-scattering effects.
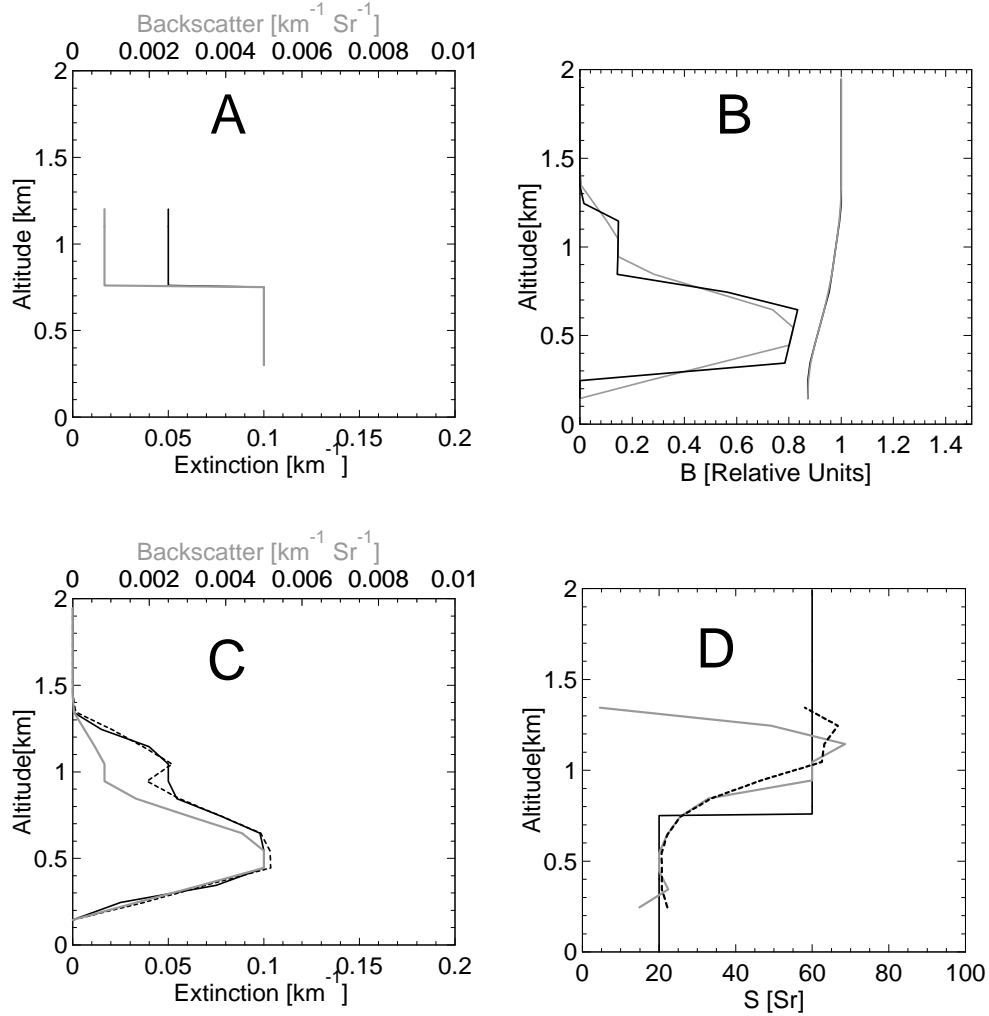
36

Figure A1. A: Profiles of model-truth extinction and backscatter. B: Attenuated Rayleigh (Right–lines) and Mie (Left–lines) backscatter profiles at 0.1 km resolution (Black) and 0.3 km (Grey). C: Retrieved backscatter (Grey-line) and retrieved extinction using the conventional log-derivative approach (Grey-solid-line) and the local-forward-modelling approach (dashed-Black-line). D: The solid-Black line corresponds to the model truth extinction-to-backscatter ratio while the Grey-solid-line represents the conventional log-derivative approach estimate while the dashed-Black-line corresponds to the result from the local-forward-modelling approach.

If one defines

$$M_p(z) = \frac{P(z)}{P_{ss}(z)} = \exp\left[2\int_0^z (1 - \eta_p(z'))\alpha(z')dr(z')\right] \qquad (B1)$$
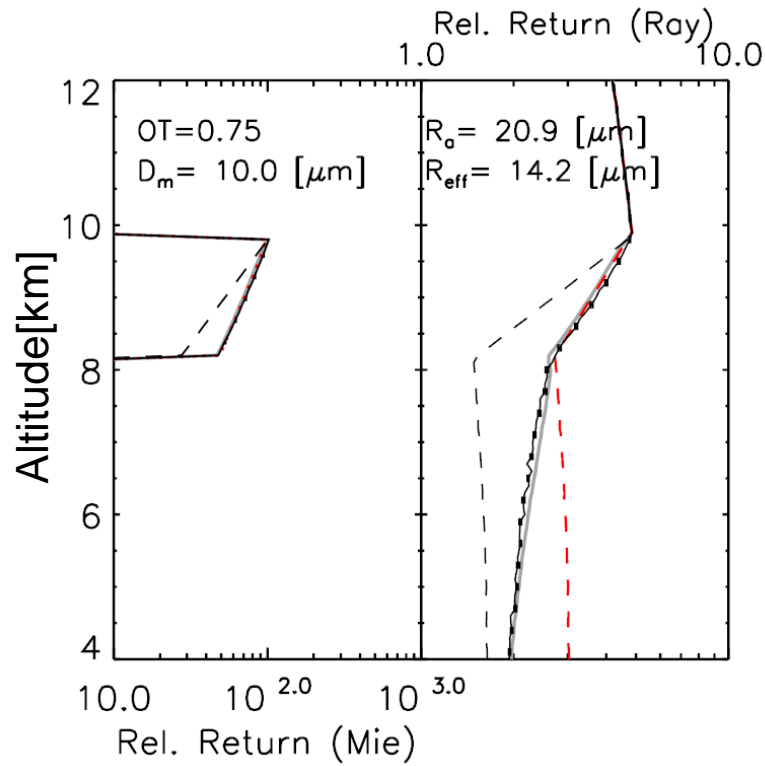
Figure B1. Sample comparison between the ECSIM lidar Monte-Carlo multiple scattering model (Donovan et al., 2023), the analytical model due to Hogan and Battaglia (2008), and Platt's equation B2. (Left) Mie co-polar and (Right) Rayleigh channel co-polar returns for an ice cloud of OT 0.75 and an effective radius of 30.7 microns. Black-solid line (with error-bars): ECSIM results. Dashed-Black line: Single scattering results. Solid Grey line: Hogan's model results for the true value of R_a. Red line: Platt's equation.

510   where M_p is the ratio of the total received power including all scattering orders (P) and the single-scatter power P_{ss}. η_p is the multiple scattering effective extinction factor such that $(1 - \eta_p)$ is the fraction of scattered energy that remains within the lidar field-of-view (and thus behaves like it has not be scattered). If one then multiplies this expression by an expression for the single-scatter lidar attenuated backscatter then Platt's multiple-scattering equation is recovered i.e.

$$B(z) = \beta(z) \exp \left[-2 \int_0^z \eta(z')\alpha(z')dr(z') \right] \tag{B2}$$

B2   The origin of MS tails

As mentioned above, Platt's approach is fast but severely limited in cases where "tails" may be present. The orgin of the tails can be simply explained. Referring to Fig. B1, within the cloud the low mean-free-path of the photons ensures that the multiple-scattered light that contributes to the detected signal tends to be confined to within the field-of-view of the lidar, however, the angular variance of the lidar beam will increase as it propagates downwards through the cloud with more and more photons undergoing scattering events.

At cloud base, the lidar beam emerges with an effective angular divergence which increases with the optical thickness of the cloud and decreases with the size of the cloud particles. This is due to that fact that the angular-width of the cloud phase function forward lobe increases with decreasing particle size i.e.

$$\theta_{sc} = \left(\frac{\lambda}{\pi R_a} \right) \tag{B3}$$

Below cloud base the lidar beam will continue to propagate with a given divergence. However, the horizontal spread of the photons is no longer constrained by the presence of the cloud. As the beam continues to propagate downwards, depending of the lidar receiver footprint more and more of the multiple-scattered photons will travel outside of the receiver cone. Though less pronounced, mainly due to the larger fov, such tails can be found in Calipso observations. Note that θ_{sc} is only defined for range-gates where particles are deemed to be present.

B3   An Extension to Platt's approach

Following the discussion in the previous section, it is apparent that the "tails" can be viewed as a decay of the signals towards single-scattering levels. Accordingly, we modify the form of the multiple-scattering ratio Eqn. B1 to allow for such decays to occur i.e.

$$M(z) = (1 - f(z)) + f(z) \exp \left[2\eta(z)\tau(z) \right] \tag{B4}$$

where $\eta = 1 - \eta_p$ (here assumed to be constant per atmospheric layer) and $f(z)$ is the range-dependent multiple scattering return signal fraction. Note that here we have replaced η_p by η for reasons of convenience, that is, η is equal to the fraction of multiply-scattering light remaining in the field-of-view (instead of $1 - \eta_p$). Note that if η is equal to zero then $M(r) = 1$ (irregardless of the values of $f(z)$) and no multiple-scattering is detected. Also, if $f(z)$ is equal to zero $M(z) = 1$ (irregardless of the values of $\eta(z)$) and if $f(z)$ is equal to 1 then Eq. (B3) reduces to Eq. (B1).

If we multiply by the single-scatter lidar attenuated backscatter expression then

$$B(z) = \beta(z) \exp \left[-2\tau(z) \right] \left((1 - f(z)) + f(z) \exp \left[2\eta(z)\tau(z) \right] \right) \tag{B5}$$

B3.1   Determination of $f(z)$

To be useful, a means to determine the profile of $f(z)$ must be established.
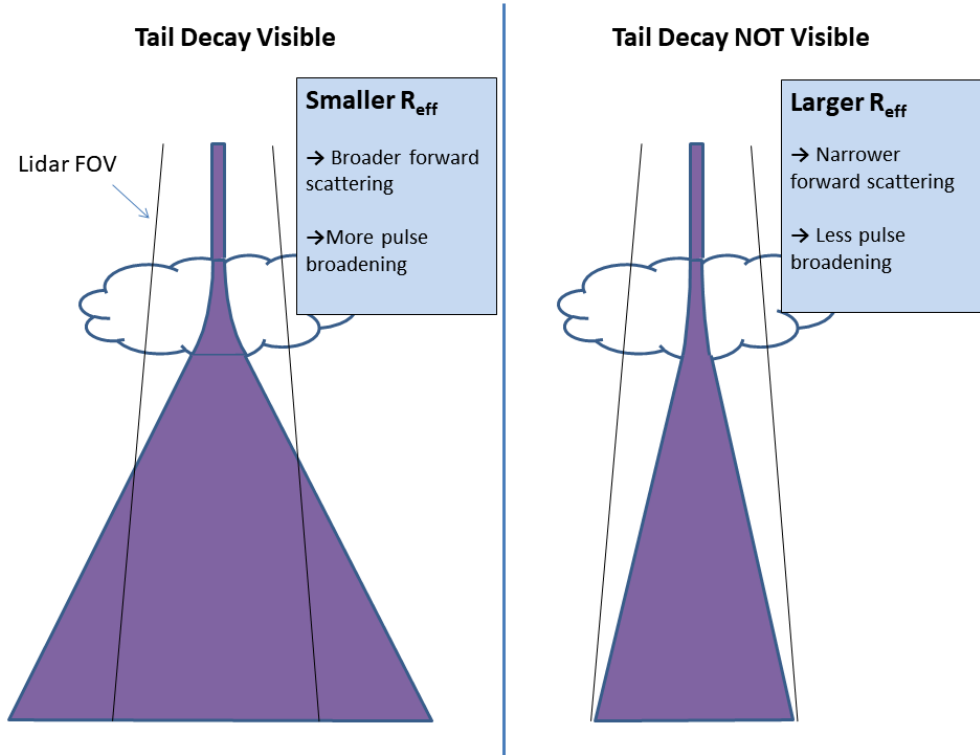
Figure B2. Schematic depiction of the mechanisms behind the occurrence of decaying tails below scattering layers. Here the Purple regions represent the broadened laser pulse extent.

We start by considering the case of a physically thin scattering layer as schematically depicted in Fig. B3 . If we assume

545 that the beam has a Gaussian profile and model the forward-scattering lobe of the effective layer phase function by a Gaussian (Eloranta, 2005), then the divergence of the forward scattered light will also be Gaussian with a divergence given by the convolution of the incoming beam divergence (θ_l) with the effective scattering forward-lobe width (θ_{Sc}) so that the effective width of the multiply scattering radiation emerging from the layer bottom is given by

$$\theta_{eff} = \left(\theta_{Sc}^2 + \theta_l^2\right)^{1/2}. \tag{B6}$$

550 By integrating the effective beam across the lidar fov the fraction of the light that remains within the fov is given by

$$f(z, z_l) = 1.0 - \exp\left[-\left(\frac{\rho_t{}^2(r(z) - r_{Sat})^2}{\theta_{sc}{}^2(r(z) - r(z_l))^2 + \theta_l{}^2(r(z) - r_{Sat})^2}\right)\right] \tag{B7}$$

where ρ_t is the receiver telescope full-angle angular fov, θ_l is the laser full-angle divergence, r_{sat} is the satellite altitude and r_l is the altitude of the scattering layer. This expression is only valid for a single thin scattering layer and so, by itself, is not so useful. However, we can generalize this expression to the case of a general profile in a heuristic approximate fashion. A
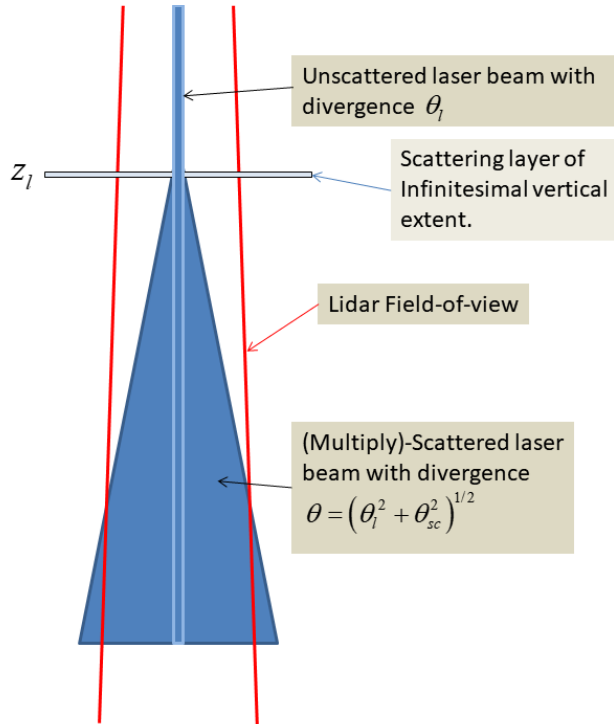
Figure B3. Schematic depiction of the angular broadening experienced by a lidar pulse as it interacts with a physically (but not optically) thin scattering layer at altitude .

555 rigorous calculation would be involved and would result in a similar formalism as the QSA model of Hogan (2008). Here we will use the information present in the signal itself to calculate the effective under general conditions. Since the observed signal itself contains information on the location and relative strength of the scattering at each level, we postulate the form (where θ_{sc} is non-zero only for those altitudes where particles are deemed to exist)

$$f_e(z) = \frac{\int_{z_{sat}}^{z} f(z, z_l) B(z) H(\theta_{sc}(z) > 0) dz_l}{\int_{z_{sat}}^{z} B(z) H(\theta_{sc}(z) > 0) dz_l} \tag{B8}$$

560 where H is the Heaviside step function and where B is the total observed attenuated backscatter. That is, we use the observed backscatter profile itself as a weighting factor to determine the effective profile. In the limit of a single thin scattering layer this expression yields the correct result.

An example comparison between Monte-Carlo calculations, Platt's approach and the "Platt+Tails" approach (Eq. (B5)) together with Eq. (B8) is shown in Fig. B4. Here a fitting procedure was used to find the best values of η and θ_{Sc} for each of the

565 two layers. It can be seen that the extended Platt approach provides a very good match to the MC results for the entire profile while the normal Platt approach is deficient.

As a further refinement, in order to account for the fact that the effective backscatter coefficient for multipley-scattering light may, in general, be lower than that than associated with single-scattering (Hogan, 2008; Wandinger, 1998; Eloranta, 1998) an additional factor is added which acts to adjust Eq. (B8) based on the relative amount of particulate scattering i.e.

$$f_{M,e}(z) = f_{Msp}(z) f_e(z).$$ (B9)

where f_{MSp} is a factor which accounts for reduced backscattering of multiply scattering light due to the existence of a backscatter peak in the particle phase functions. It was previously thought that ice particles would not posses a strong backscatter peak. However, newer results indicate that that even irregular and rough crystals will possess a backscatter peak (Zhou and Yang, 2015). Molecular Rayleigh scattering possesses an effectively isotropic phasefunction in the backscatter direction, thus no adjustment is necessary for the Rayleigh scattering.

Putting all the above elements together we have, specific for calibrated crosstalk corrected attenuated backscatters

$$B_M(z) = \beta_M(z) e^{-2\tau(z)} \left[(1 - f_e(z)) + f_{M,e}(z) e^{2\tau_\eta(z)} \right]$$ (B10)

$$B_R(z) = \beta_R(z) e^{-2\tau(z)} \left[(1 - f_e(z)) + f_e(z) e^{2\tau_\eta(z)} \right]$$ (B11)

,

where τ and τ_η are given by

$$\tau(z) = \int_{z_{sat}}^{z} (\alpha_R(z') + \alpha_M(z')) dz'$$ (B12)

and

$$\tau_\eta(z) = \int_{z_{sat}}^{z} \eta(z') \alpha_M(z') dz'.$$ (B13)

A number of single-layer Monte-Carlo based simulations similar to that depicted in Fig. B4 for as range of ice cloud, water cloud and aerosol layers were conducted that indicated that specifying η to be equal to 0.45–0.5 for both water and ice clouds, 0.375 for Dust and Sea salt and 0.1 for general aerosol types. In should be noted that, for small effective radii scatterers that η is not very important for determining the signal-profiles as f remains small.

B4   MS extinction and backscatter corrections

Using a forward-modeling approach based on Eq. B8, multiple-scattering effects, including the effects of "tails" can be accounted for. For *local-methods* employed to estimate the extinction, such as the approaches described in Section A other *correction* type approaches are useful. In the following two sections the methods used to correct for multiple-scattering effects are described.
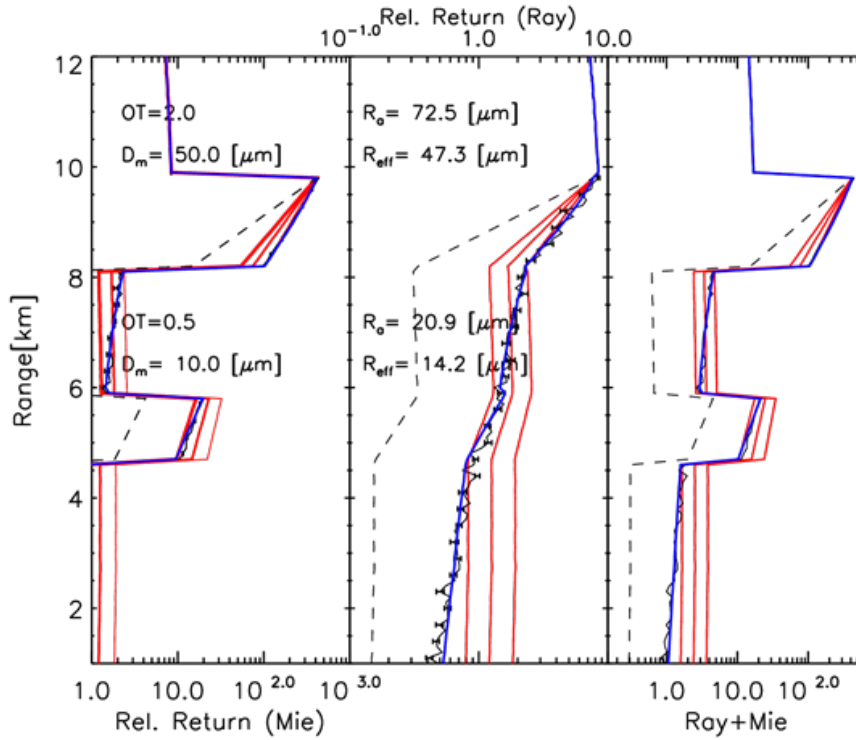
Figure B4. From Left to Right: Total simulated total attenuated backscatter, Rayleigh attenuated backscatter profile and the total simulated attenuated backscatter profile (difference scale than the first columns) corresponding to a two-layer ice cloud system with the given layer parameters. The Black lines (with the error-bars) are the product of lidar Monte-Carlo radiative transfer calculations. The Dotted back lines are the single-scatter return values, the Red lines are the results of Platt's approach using tree different values of η (0.4,0.5,0.6). The Blue-lines show the result of applying Eq. (B5) together with Eq. (B8) together with optimally chosen of values of η and θ_{Sc} for each of the two layers.

B4.1 Extinction

First, focusing on the extinction, starting with Eq. (B11) we can write

$$B_R^{Rat}(z) = \frac{B_M(z)}{\beta_R(z)} exp[2\tau_R] = e^{-2\tau(z)} \left[(1 - f_e(z)) + f_e(z) e^{2\tau_\eta(z)} \right] \tag{B14}$$

Taking the log of Eq. B14 then yields

$$\log B_R^{Rat}(z) = -2\tau(z) + \log \left[(1 - f_e(z)) + f_e(z) e^{2\tau_\eta(z)} \right] \tag{B15}$$

then taking the derivative with range leads to

$$\frac{\log B_R^{Rat}}{dz}(z) = -2\alpha_M(z) + \frac{\left(e^{2\tau_\eta(z)} - 1\right)\frac{df_e}{dr}(z) + 2f_e(z)\eta(z)\alpha_M(z)e^{2\tau_\eta(z)}}{(1 - f_e(z)) + f_e(z)e^{2\tau_\eta(z)}} \tag{B16}$$

600 Now, if we define the *effective* extinction (i.e. the extinction that would be estimated assuming that no multiple scattering was occurring) as

$$\alpha_M^e(z) = -\frac{1}{2}\frac{\log B_R^{Rat}}{dr}(z) \tag{B17}$$

then

$$\alpha_M(z) = \alpha_M^e(z) + \frac{1}{2}\frac{\left(e^{2\tau_\eta(z)} - 1\right)\frac{df_e}{dr}(z) + 2f_e(z)\eta(z)\alpha_M(z)e^{2\tau_\eta(z)}}{(1 - f_e(z)) + f_e(z)e^{2\tau_\eta(z)}}. \tag{B18}$$

605 Eq. B18 can easily be solved iteratively as folows:

1. The η and Ra profiles must first be specified.

2. The $f(z)$ profile (and it's derivative) is calculated by using Eq. B8.

3. The effective extinction is calculated using Eq. B17

4. τ_η is calculated using $\alpha_M^e(z)$ as a first guess for α_M.

610 5. α_M is updated using Eq. B18.

6. τ_η is calculated using α_M

7. Steps 5 and 6 are repeated until convergence (typically 2-3 times).

In order to estimate the error, for simplicity it is assumed that the uncertainty in α_M is dominated by the uncertainty in α_M^e.

The application of Eq. B18 is illustrated by Figures B5 and B6. Here four cases of homogeneous layers were considered

615 covering a range of conditions from low extinction ($\alpha_M = 0.1$ km^{-1}) to high extinction ($\alpha_M = 1.0$ km^{-1}) and small and larger particles sizes respectively. A satellite altitude of 400 km was assumed, the laser divergence was set to

Referring to Figs. B5 and B6, it can be seen that in all the cases considered, that the P+T approach can provide a good match to the the results generated by the approach of Hogan B8 if η is set to a value of 0.425. Also it can be seen that the extinction estimates made using Eq. B18 are accurate to within under 10 % (here 3 iterations were used) while the estimates

620 made neglecting multiple-scattering or using Platt's approach are subject to much larger errors in general.

B4.2 Backscatter

Now considering the backscatter. The observed(effective) backscatter can be related to the ratio of the Mie and Rayleigh attenuated backscatters i.e. using Eqns. B11 and B10,

$$\beta_M^e(z) = \beta_R(z)\left(\frac{B_M}{B_R}\right) \tag{B19}$$

625

$$= \beta_M \frac{\left[(1 - f_e(z)) + f_{M,e}(z)e^{2\tau_\eta(z)}\right]}{\left[(1 - f_e(z)) + f_e(z)e^{2\tau_\eta(z)}\right]}. \tag{B20}$$

When multiple scattering is not important (i.e. $f_e(z) = 0$ or $\tau_\eta(z) = 0$) then $\beta_M^e(z) = \beta_M(z)$. However, when multiple scattering is important (i.e. $f_e(z) = 1$ or $2\tau_{eta}(z) >> 1$)) then $\beta_M^e(z) = f_{M,e}(z)\beta_M(z)$. Once the extinction profile has been determined as was described in the previous section, then the appropriate adjustment for multiple-scattering can be calculate directly using Eq. B20.

B4.3 Sensitivity

The accuracy of the procedures described in Sections B4.1 and B4.2 is on the order of a few percent if the correct values of Ra, η and f_{MSp} are employed. However, this will not be the case in general. In order to assess the magnitude of the errors that may be expected due to the uncertainties in Ra, η and f_{MSp}, the simple simulated cases shown in Fig. B5 and Fig. B6 were inverted and corrected for multiple-scattering effects using Eqns. (B18) and but using values of Ra, η and f_{MSp} different from the model-truth values.

Example of the impact of the particle size are shown in Fig. B8 and Fig. B9. Here it can be seen that halving the values of the effective area radius leads to an underestimation of the extinction by about 10-15% near the later top while doubling the effective area radius leads to an overestimation of the same rough magnitude. The corresponding errors in the lidar-ratio follow the same pattern with somewhat higher percentage values.

The relative errors resulting from errors in Ra do not depend strongly on the extinction itself however, they can be strongly dependent on Ra. When Ra is such that the associated θ_{sc} is much larger or smaller than ρ_t then the impact of specifying Ra is limited. This is illustrated by Fig. B9, where it can be seen that halving the value of Ra used in the MS correction has a limited effect (less than 10% at the layer bottom) on the estimated extinction and lidar-ratio while doubling the value of Ra used has practically no effect (since both 25 and $50\mu m$ produce a small value of θ_{sc} compared to ρ_t.

The values of f_{MSp} used for the MS correction procedure do not impact the retrieved extinction, however, the retrieved backscatter (and hence the estimated lidar-ratio) will be impacted. In the limiting case where f is close to 1, then the relative errors in the retrieved backscatter (and associated lidar-ratio) will directly correspond to the relative error in the value of f_{MSp} used in the inversion.

The sensitivity of the corrections to the assumed value of η were also investigated using trials values of $0.4 and 0.45$. In all of the cases the impact was below 10% for both the extinction and lidar-ratio.

In summary, within layers, if the particle sizes care accurate within a factor of two, maximum errors in the extinction and lidar-ratio on the order of 10-15 % may be expected. The uncertainty in f_{MSp} likely adds another 10-15% to the uncertainty in the lidar-ratio determination. For spherical scatterers, f_{MSp} can be calculated using exact phase functions calculated using Mie theory (Hogan and Battaglia, 2008; Eloranta, 1998). For ice clouds, there is evidence for the general existence of a more pronounced backscatter-peak (which implies values of f_{MSp} significantly less than 1) even for irregular crystals (Zhou and Yang, 2015).

The above conclusions are relevant for single-layer situations. In the case of e.g. semi-transparent cirrus above aerosols, the sensitivity to especially the particle size can be more significant. This aspect is discussed in Section 3 where specific cases drawn from the GEM-ECSIM test scenes are discussed.

Appendix C: A-EBD forward model and Jacobian

In this Section, the explicit form of the forward model used by the A-EBD optimal estimation retrieval is presented along with its Jacobian.

For $i \leq n$ we have, based on a discrete form of Eq. (B11),

$$F_i = B_R(z)e^{2\tau_R(z)} = B_{R,i}^c \tag{C1}$$

$$= \frac{C_{lid}}{\Delta r_i}e^{2\tau_{R,i}} \int_{r_{i,mid}-\Delta r/2}^{r_{i,mid}+\Delta r/2} \beta_R(z')e^{-2\tau(z')}\left[(1-f_e(z')) + f_e(z')e^{2\tau_\eta(z')}\right]dr(z')$$

where

$$\tau_{R,i} = \sum_{j=1}^{j=i-1} \alpha_{R,j}\Delta r_j, \tag{C2}$$

$$\tau(z') = \sum_{j=1}^{j=i-1} (\alpha_{M,j} + \alpha_{R,j})\Delta r_j + (\alpha_{M,i} + \alpha_{R,i})(r(z) - r_{i-1}) \tag{C3}$$

$$\tau_\eta(z') = \sum_{j=1}^{j=i-1} (\eta_j \alpha_{M,j})\Delta r_j + (\eta_i \alpha_{M,i}(r(z') - r_{i-1}), \tag{C4}$$

and f_e is the discrete version of Eq.(B9).

For $i > n$ we have, based on a discrete form of Eq. (B10),

$$F_i = B_M(z)e^{2\tau_R(z)} = B_{M,i}^c \tag{C5}$$

$$= \frac{C_{lid}}{\Delta r_i}e^{2\tau_{R,i}} \int_{r_{i,mid}-\Delta r/2}^{r_{i,mid}+\Delta r/2} S^{-1}(z')\alpha_M(z')e^{-2\tau(z')}\left[(1-f_e(z')) + f_{M,e}(z')e^{2\tau_\eta(z')}\right]dr(z').$$

Assuming that for each range-bin, that the Mie and Rayleigh extinctions, lidar-ratio, and f terms can be treated as being constant, evaluating the integral in Eq. (C1) then yields, for the Rayleigh signal forward model,

$$B_{R,i}^c = C_{lid}\beta_{R,i}\left[\Delta z_{c_1,i}(1-f_{e,i}) + \Delta z_{c_2,i}f_{e,i}e^{2\tau_{\eta,i}}\right] \tag{C6}$$

and for the Mie signal forward model,

$$B_{M,i}^c = C_{lid}\frac{\alpha_{M,i}}{S_i}\left[\Delta z_{c_1,i}(1-f_{e,i}) + \Delta z_{c_2,i}f_{M,e,i}e^{2\tau_{\eta,i}}\right] \tag{C7}$$

where

$$\Delta z_{c_1,i} = \frac{1 - \exp\left[-2(\alpha_{M,i} + \alpha_{R,i})\Delta r_i\right]}{2(\alpha_{M,i} + \alpha_{R,i})\Delta r_i} \tag{C8}$$

685 and

$$\Delta z_{c_2,i} = \frac{1 - \exp\left[-2(\alpha_{M,i}(1.0-\eta_i)+\alpha_{R,i})\Delta r_i\right]}{2\left(\alpha_{M,i}(1.0-\eta_i)+\alpha_{R,i}\right)\Delta r_i} \tag{C9}$$

C1 Gradient and Jacobian elements

In order to efficiently minimize the cost function, we must be able to compute its gradient with respect to the elements of the state vector. The gradient of the cost-function is related to the Jacobian of the forward model as:

690 $$\nabla\chi^2 = -2\mathbf{J}^T\mathbf{S_e}^{-1}\left(\mathbf{y}-\mathbf{F}(\mathbf{x})\right)+2\mathbf{S_a}^{-1}\left(\mathbf{x_r^l}-\mathbf{x_a^l}\right), \tag{C10}$$

where $\mathbf{J}$ is the forward model Jacobian with respect to the log state variables i.e.

$$
\begin{aligned}
J_{i,j} &= \frac{\partial F_i(\mathbf{x})}{\partial x_j^l} \\
&= \frac{\partial F_i(\mathbf{x})}{\partial \log_{10}(x_j)} = \frac{\partial F_i(\mathbf{x})}{\partial x_j}\frac{\partial x_j}{\partial \log_{10}(x_j)} = \frac{\partial F_i(\mathbf{x})}{\partial x_j}\log_e(10)x_j.
\end{aligned}
\tag{C11}
$$

695

C1.1 Derivatives with respect to extinction.

Using the forward model the partial derivatives with respect to the particulate extinctions are:

for $j < i; i \leq n_z$

$$
\begin{aligned}
\frac{\partial F_i(\mathbf{x})}{\partial x_j} &= \frac{\partial B_{R,i}^c(\mathbf{x})}{\partial \alpha_j} \\
&= 2C_{lid}\beta_{R,i}\left(\Delta z_{c_1,i}\exp\left[-2\tau_i\right](f_{e,i}-1)\Delta r_j + \Delta z_{c_2,i}f_{e,i}\exp\left[2(\tau_{\eta,i}-\tau_i)\right]\Delta r_j(\eta_j-1)\right).
\end{aligned}
\tag{C12}
$$

For $i = j; i \leq n_z$

$$
\begin{aligned}
\frac{\partial F_i(\mathbf{x})}{\partial x_i} &= \frac{\partial B_{R,i}^c(\mathbf{x})}{\partial \alpha_i} \\
&= C_{lid}\beta_{R,i}\left(\frac{\partial\Delta z_{c_1,i}}{\partial\alpha_i}\exp\left[-2\tau_i\right](1-f_{e,i}) + \frac{\partial\Delta z_{c_2,i}}{\partial\alpha_i}f_{e,i}\exp\left[2\tau_{\eta,i}-2\tau_i\right]\right)
\end{aligned}
\tag{C13}
$$

where

705 $$\frac{\partial\Delta z_{c_1,i}}{\partial\alpha_i} = -\frac{\Delta z_{c_1,i} + \exp\left[-2(\alpha_{M,i}+\alpha_{R,i})\right]\Delta r_i}{\alpha_{M,i}+\alpha_{R,i}} \tag{C14}$$

and

$$\frac{\partial\Delta z_{c_2,i}}{\partial\alpha_i} = \frac{(2\exp\left[-2(\alpha_{M,i}+\alpha_{R,i})\right]\Delta r_i - 1)(1-\eta_i)\Delta r_i}{(2(\alpha_{M,i}(1-\eta_i)+\alpha_{R,i})\Delta r_i)^2} + \frac{(1-\eta_{M,i})\exp\left[-2(\alpha_{M,i}+\alpha_{R,i})\right]\Delta r_i}{\alpha_{M,i}(1-\eta_i)+\alpha_{R,i}}. \tag{C15}$$

For $j < i; n_z < k \leq 2n_z; k = n_z + i$

$$
\begin{aligned}
\frac{\partial F_k(\mathbf{x})}{\partial x_j} &= \frac{\partial B_{M,i}^c(\mathbf{x})}{\partial \alpha_j} \\
&= 2C_{lid}\frac{\alpha_{M,i}}{S_i}\left(\Delta z_{c_1,i}\exp\left[-2\tau_i\right]\left(f_{e,i}-1\right)\Delta r_j + \Delta z_{c_2,i}f_{M,e,i}\exp\left[2(\tau_{\eta,i}-\tau_i)\right]\Delta r_j(\eta_j-1)\right),
\end{aligned}
\tag{C16}
$$

and For $j = i; n_z < k \leq 2n_z; k = n_z + i$

$$
\begin{aligned}
\frac{\partial F_k(\mathbf{x})}{\partial x_i} &= \frac{\partial B_{M,i}^c(\mathbf{x})}{\partial \alpha_i} \\
&= \frac{B_{M,i}^c}{\alpha_i} + C_{lid}\frac{\alpha_{M,i}}{S_i}\left(\frac{\partial \Delta z_{c_1,i}}{\partial \alpha_i}\exp\left[-2\tau_i\right]\left(1-f_{e,i}\right) + f_{M,e,i}\frac{\partial \Delta z_{c_2,i}}{\partial \alpha_i}\exp\left[2(\tau_{\eta,i}-\tau_i)\right]\right).
\end{aligned}
\tag{C17}
$$

Derivatives with respect to lidar-ratio.

For the lidar-ratio elements of the state-vector, one must take into account that the state-vector elements represent extended layers. Thus,

$$
\frac{\partial F_i(\mathbf{x})}{\partial x_l} = \sum_{j=j_{b,l}}^{j_{t,l}} \frac{\partial B_{R,i}^c(\mathbf{x})}{\partial S_j}
\tag{C18}
$$

where $n_z < l < n_z + n_l$ and $i \leq n_z$. $j_{t,j}$ is the range-index of the layer top for the layer corresponding to the lth element of the state-vector and $j_{b,j}$ is the range-index of the layer top for the layer corresponding to the lth element of the state-vector.

For $n_z < i \leq 2n_z$

$$
\frac{\partial F_i(\mathbf{x})}{\partial x_l} = \sum_{j=j_{b,l}}^{j_{t,l}} \frac{\partial B_{M,i}^c(\mathbf{x})}{\partial S_j}
\tag{C19}
$$

For $j < i$

$$
\frac{\partial B_{M,i}^r(\mathbf{x})}{\partial S_j} = 0
\tag{C20}
$$

and for $i = j$

$$
\frac{\partial B_{M,i}^r(\mathbf{x})}{\partial S_i} = -\frac{B_{M,i}^r}{S_i}.
\tag{C21}
$$

C1.2 Derivatives with respect to particle-size.

For the R_a elements of the state-vector, as is the case for thee lidar-ratio, one must take into account that the state-vector elements represent extended layers. Thus,

$$
\frac{\partial F_i(\mathbf{x})}{\partial x_l} = \sum_{j=j_{b,l}}^{j_{t,l}} \frac{\partial B_{R,i}^c(\mathbf{x})}{\partial \theta_j}\frac{\partial \theta_j}{\partial R_{a,j}}
\tag{C22}
$$

where $2n_z < l < n_z + 3n_l$ and $i \leq n_z$ and

$$\frac{\partial \theta_j}{\partial R_{a,j}} = -\frac{\lambda}{\pi R_{a,j}^2}. \tag{C23}$$

For $j \leq i$

$$\frac{\partial B_{R,i}^c(\mathbf{x})}{\partial \theta_j} = C_{lid}\beta_{R,i}\left(\Delta z_{c_2,i}\exp\left[2(\tau_{\eta,i} - \tau_i)\right] - \Delta z_{c_1,i}\exp\left[-2\tau_i\right]\right)\frac{\partial f_{e,i}}{\partial \theta_j}, \tag{C24}$$

where

$$\begin{aligned}
\frac{\partial f_{e,i}}{\partial \theta_j} &= \left[-2\left(B_{M,j} + B_{R,j}\right)\exp\left[-\frac{(r_i\rho_t)^2}{(r_i\rho_l)^2 + (\theta_j^2(r_i - r_j)^2}\right]\Delta r_j\left[\frac{(r_i\rho_t)^2}{\left[(r_i\rho_l)^2 + \theta_j^2(r_i - r_j)^2\right]^2}\right]\theta_j(r_i - r_j)^2\right] \\
&\times \left[\sum_{k=0}^{i}H(\theta_k > 0)\left(B_{M,k} + B_{R,k}\right)\Delta r_k\right]^{-1}. \tag{C25}
\end{aligned}$$

For $n_z < i \leq 2n_z$,

$$\frac{\partial F_i(\mathbf{x})}{\partial x_l} = \sum_{j=j_{b,l}}^{j_{t,l}}\frac{\partial B_{M,i}^c(\mathbf{x})}{\partial \theta_j}\frac{\partial \theta_j}{\partial R_{a,j}} \tag{C26}$$

For $j \leq n_z$

$$\frac{\partial B_{M,i}^c(\mathbf{x})}{\partial \theta_j} = C_{lid}\alpha_{M,i}S_i^{-1}\left(\Delta z_{c_2,i}\exp\left[2(\tau_{\eta,i} - \tau_i)\right] - \Delta z_{c_1,i}\exp\left[-2\tau_i\right]\right)\frac{\partial f_{M,e,i}}{\partial \theta_j}. \tag{C27}$$

C1.3 Derivatives with respect to C_{lid}.

For $j = n_z + 2n_l + 1$ and $i \leq n_z$

$$\frac{\partial F_i(\mathbf{x})}{\partial x_j} = \frac{\partial B_{R,i}^c(\mathbf{x})}{\partial C_{lid}} = \frac{B_{R,i}^c}{C_{lid}} \tag{C28}$$

and for $n_z < i \leq 2n_z$

$$\frac{\partial F_i(\mathbf{x})}{\partial x_j} = \frac{\partial B_{M,i}^c(\mathbf{x})}{\partial C_{lid}} = \frac{B_{R,i}^c}{C_{lid}} \tag{C29}$$

References

J. P. do Carmo, A. Hélière, L. Le Hors, Y. Toulemont, A. Lefebvre, and A. Lefebvre. ATLID, ESA Atmospheric LIDAR Developement
    Status. *EPJ Web of Conferences*, 119:04003, 6 2016. ISSN 2100-014X. https://doi.org/10.1051/epjconf/201611904003. URL http:
    //www.epj-conferences.org/10.1051/epjconf/201611904003.

J. P. do Carmo, G. de Villele, K. Wallace, A. Lefebvre, K. Ghose, T. Kanitz, F. Chassat, B. Corselle, T. Belhadj, and P. Bravetti. Atmospheric
    lidar (atlid): Pre-launch testing and calibration of the european space agency instrument that will measure aerosols and thin clouds in
    the atmosphere. *Atmosphere*, 12(1), 2021. ISSN 2073-4433. https://doi.org/10.3390/atmos12010076. URL https://www.mdpi.com/
    2073-4433/12/1/76.

D. P. Donovan, H. Klein Baltink, J. S. Henzing, S. R. de Roode, and A. P. Siebesma. A depolarisation lidar-based method for the determination
    of liquid-cloud microphysical properties. *Atmospheric Measurement Techniques*, 8(1):237–266, 2015. https://doi.org/10.5194/amt-8-237-
    2015. URL https://amt.copernicus.org/articles/8/237/2015/.

D. P. Donovan, P. Kollias, A. Velázquez Blázquez, and G.-J. van Zadelhoff. The generation of earthcare l1 test data sets using atmospheric
    model data sets. *Atmospheric Measurement Techniques*, 16(21):5327–5356, 2023. https://doi.org/10.5194/amt-16-5327-2023. URL
    https://amt.copernicus.org/articles/16/5327/2023/.

M. Eisinger, T. Wehr, T. Kubota, D. Bernaerts, and K. Wallace. The EarthCARE production model and auxiliary products. *Atmospheric
    Measurement Techniques*, to be submitted, 2022.

M. Eisinger, F. Marnas, K. Wallace, T. Kubota, N. Tomiyama, Y. Ohno, T. Tanaka, E. Tomita, T. Wehr, and D. Bernaerts. The earthcare
    mission: Science data processing chain overview. *EGUsphere*, 2023:1–35, 2023. https://doi.org/10.5194/egusphere-2023-1998. URL
    https://egusphere.copernicus.org/preprints/2023/egusphere-2023-1998/.

E. Eloranta. Lidar: Range-resolved optical remote sensing of the atmosphere. *High Spectral Resolution Lidar*, pages 143–163, 2005.

E. W. Eloranta. Practical model for the calculation of multiply scattered lidar returns. *Appl. Opt.*, 37(12):2464–2472, Apr 1998.
    https://doi.org/10.1364/AO.37.002464. URL https://opg.optica.org/ao/abstract.cfm?URI=ao-37-12-2464.

A. Heymsfield, D. Winker, M. Avery, M. Vaughan, G. Diskin, M. Deng, V. Mitev, and R. Matthey. Relationships between ice water content
    and volume extinction coefficient from in situ observations for temperatures from 0° to -86°c: Implications for spaceborne lidar retrievals.
    Journal of Applied Meteorology and Climatology, 53(2):479 – 505, 2014a. https://doi.org/10.1175/JAMC-D-13-087.1. URL https://
    journals.ametsoc.org/view/journals/apme/53/2/jamc-d-13-087.1.xml.

A. Heymsfield, D. Winker, M. Avery, M. Vaughan, G. Diskin, M. Deng, V. Mitev, and R. Matthey. Relationships between ice water content
    and volume extinction coefficient from in situ observations for temperatures from 0° to -86°c: Implications for spaceborne lidar retrievals.
    Journal of Applied Meteorology and Climatology, 53(2):479 – 505, 2014b. https://doi.org/https://doi.org/10.1175/JAMC-D-13-087.1.
    URL https://journals.ametsoc.org/view/journals/apme/53/2/jamc-d-13-087.1.xml.

A. J. Heymsfield, D. Winker, and G.-J. van Zadelhoff. Extinction-ice water content-effective radius algorithms for calipso. *Geophysical
    Research Letters*, 32(10), 2005. https://doi.org/https://doi.org/10.1029/2005GL022742. URL https://agupubs.onlinelibrary.wiley.com/
    doi/abs/10.1029/2005GL022742.

R. J. Hogan. Fast Lidar and Radar Multiple-Scattering Models. Part I: Small-Angle Scattering Using the Photon Variance–Covariance
    Method. *Journal of the Atmospheric Sciences*, 65(12):3621–3635, 12 2008. ISSN 0022-4928. https://doi.org/10.1175/2008JAS2642.1.
    URL http://journals.ametsoc.org/doi/abs/10.1175/2008JAS2642.1.

R. J. Hogan and A. Battaglia. Fast Lidar and Radar Multiple-Scattering Models. Part II: Wide-Angle Scattering Using the Time-
Dependent Two-Stream Approximation. *Journal of the Atmospheric Sciences*, 65(12):3636–3651, 12 2008. ISSN 0022-4928.
https://doi.org/10.1175/2008JAS2643.1. URL http://journals.ametsoc.org/doi/abs/10.1175/2008JAS2643.1.

Y. Hu, D. Winker, M. Vaughan, B. Lin, A. Omar, C. Trepte, D. Flittner, P. Yang, S. L. Nasiri, B. Baum, R. Holz, W. Sun, Z. Liu, Z. Wang,
S. Young, K. Stamnes, J. Huang, and R. Kuehn. Calipso/caliop cloud phase discrimination algorithm. *Journal of Atmospheric and
Oceanic Technology*, 26(11):2293 – 2309, 2009. https://doi.org/10.1175/2009JTECHA1280.1. URL https://journals.ametsoc.org/view/
journals/atot/26/11/2009jtecha1280_1.xml.

A. J. Illingworth, H. W. Barker, A. Beljaars, M. Ceccaldi, H. Chepfer, N. Clerbaux, J. Cole, J. Delanoë, C. Domenech, D. P. Donovan,
S. Fukuda, M. Hirakata, R. J. Hogan, A. Huenerbein, P. Kollias, T. Kubota, T. Nakajima, T. Y. Nakajima, T. Nishizawa, Y. Ohno,
H. Okamoto, R. Oki, K. Sato, M. Satoh, M. W. Shephard, A. Velázquez-Blázquez, U. Wandinger, T. Wehr, and G.-J. van Zadelhoff.
The EarthCARE Satellite: The Next Step Forward in Global Measurements of Clouds, Aerosols, Precipitation, and Radiation. *Bulletin of
the American Meteorological Society*, 96(8):1311–1332, 8 2015. ISSN 0003-0007. https://doi.org/10.1175/BAMS-D-12-00227.1. URL
http://journals.ametsoc.org/doi/abs/10.1175/BAMS-D-12-00227.1.

A. Irbah, J. Delanoë, G.-J. van Zadelhoff, D. P. Donovan, P. Kollias, B. Puigdomènech Treserras, S. Mason, R. J. Hogan, and A. Tatarevic. The
classification of atmospheric hydrometeors and aerosols from the earthcare radar and lidar: the a-tc, c-tc and ac-tc products. *Atmospheric
Measurement Techniques*, 16(11):2795–2820, 2023. https://doi.org/10.5194/amt-16-2795-2023. URL https://amt.copernicus.org/articles/
16/2795/2023/.

A. Kliewer, S. Fletcher, A. Jones, and J. Forsythe. Comparison of gaussian, logarithmic transform and mixed gaussian-lognormal distribution-
based 1dvar microwave temperature-water vapor mixing ratio retrievals. *Quarterly Journal of the Royal Meteorological Society*, 142, 08
2015. https://doi.org/10.1002/qj.2651.

S. L. Mason, J. N. S. Cole, N. Docter, D. P. Donovan, R. J. Hogan, A. Hünerbein, P. Kollias, B. Puigdomènech Treserras, Z. Qu, U. Wandinger,
and G.-J. van Zadelhoff. An intercomparison of earthcare cloud, aerosol and precipitation retrieval products. *EGUsphere*, 2023:1–34,
2023. https://doi.org/10.5194/egusphere-2023-1682. URL https://egusphere.copernicus.org/preprints/2023/egusphere-2023-1682/.

C. M. R. Platt. Infrared absorption and liquid water content in stratocumulus clouds. *Quarterly Journal of the Royal Meteorological Society*,
102(433):553–561, 7 1976. ISSN 00359009. https://doi.org/10.1002/qj.49710243305. URL http://onlinelibrary.wiley.com/doi/10.1002/
qj.49710243305/abstracthttp://doi.wiley.com/10.1002/qj.49710243305.

C. M. R. Platt. Remote sounding of high clouds. iii: Monte carlo calculations of multiple-scattered lidar returns. *Journal of Atmospheric
Sciences*, 38(1):156 – 167, 1981. https://doi.org/https://doi.org/10.1175/1520-0469(1981)038<0156:RSOHCI>2.0.CO;2. URL https:
//journals.ametsoc.org/view/journals/atsc/38/1/1520-0469_1981_038_0156_rsohci_2_0_co_2.xml.

W. H. Press, S. A. Teukolsky, W. T. Vetterling, and B. P. Flannery. *Numerical Recipes 3rd Edition: The Art of Sci-
entific Computing*. Cambridge University Press, 3 edition, 2007. ISBN 0521880688. URL http://www.amazon.com/
Numerical-Recipes-3rd-Scientific-Computing/dp/0521880688/ref=sr_1_1?ie=UTF8&s=books&qid=1280322496&sr=8-1.

Z. Qu, D. P. Donovan, H. W. Barker, J. N. S. Cole, M. W. Shephard, and V. Huijnen. Numerical model generation of test frames for pre-launch
studies of earthcare's retrieval algorithms and data management system. *Atmospheric Measurement Techniques*, 16(20):4927–4946, 2023.
https://doi.org/10.5194/amt-16-4927-2023. URL https://amt.copernicus.org/articles/16/4927/2023/.

Straume, A.G., Rennie, M., Isaksen, L., de Kloe, J., Marseille, G.-J., Stoffelen, A., Flament, T., Stieglitz, H., Dabas, A., Huber, D., Reitebuch,
O., Lemmerz, C., Lux, O., Marksteiner, U., Weiler, F., Witschas, B., Meringer, M., Schmidt, K., Nikolaus, I., Geiss, A., Flamant, P., Kanitz,
T., Wernham, D., von Bismarck, J., Bley, S., Fehr, T., Floberghagen, R., and Parinello, T. Esa's space-based doppler wind lidar mission ae-

olus – first wind and aerosol product assessment results. *EPJ Web Conf.*, 237:01007, 2020. https://doi.org/10.1051/epjconf/202023701007. URL https://doi.org/10.1051/epjconf/202023701007.

G.-J. van Zadelhoff, D. P. Donovan, and P. Wang. Detection of aerosol and cloud features for the earthcare lidar atlid: the a-fm product. *Atmospheric Measurement Techniques*, to be submitted, 2023.

U. Wandinger. Multiple-scattering influence on extinction- and backscatter-coefficient measurements with raman and high-spectral-resolution lidars. *Appl. Opt.*, 37(3):417–427, Jan 1998. https://doi.org/10.1364/AO.37.000417. URL https://opg.optica.org/ao/abstract.cfm?URI=ao-37-3-417.

U. Wandinger, A. A. Floutsi, H. Baars, M. Haarig, A. Ansmann, A. Hünerbein, N. Docter, D. Donovan, G.-J. van Zadelhoff, S. Mason, and J. Cole. Heteac – the hybrid end-to-end aerosol classification model for earthcare. *Atmospheric Measurement Techniques*, 16(10): 2485–2510, 2023. https://doi.org/10.5194/amt-16-2485-2023. URL https://amt.copernicus.org/articles/16/2485/2023/.

D. Winker. Accounting for multiple scattering in retrievals from space lidar. *SPIE*, 5059, 04 2003. https://doi.org/10.1117/12.512352.

C. Zhou and P. Yang. Backscattering peak of ice cloud particles. *Opt. Express*, 23(9):11995–12003, May 2015. https://doi.org/10.1364/OE.23.011995. URL https://opg.optica.org/oe/abstract.cfm?URI=oe-23-9-11995.
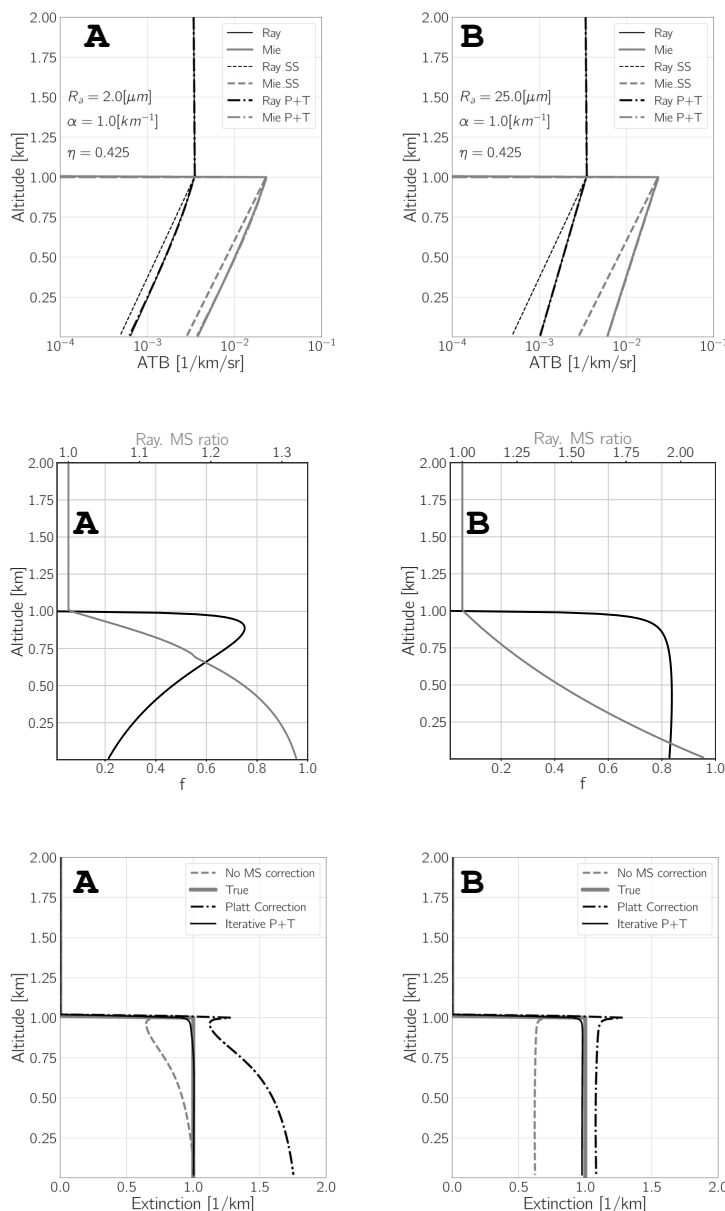
Figure B5. Results of idealized simulations using homogeneous layers. The top-panels show the Rayleigh and Mie attenuated backscatters assuming single-scattering ('Ray_SS' and 'Mie_SS' respectively) as well as the profiles generated using the approach due to Hogan ('Ray' and 'Mie' respectively) and the 'P+T' approach with $\eta = 0.425$. The middle panels show the f profiles generated using B8 and the ratio between the Rayleigh ATBs including multiple-scattering and the single-scattering ATBs. The bottom-left panels show the model-truth extinction profile, the retrieved extinction profiles assuming no multiple-scattering effects, the extinction values that would be estimated using Platt's approach and the results of iteratively applying Eq. B18. The 'A' panels correspond to the case where $R_a = 2[\mu m]$ while the 'B' panels correspond to the case where $R_a = 25[\mu m]$
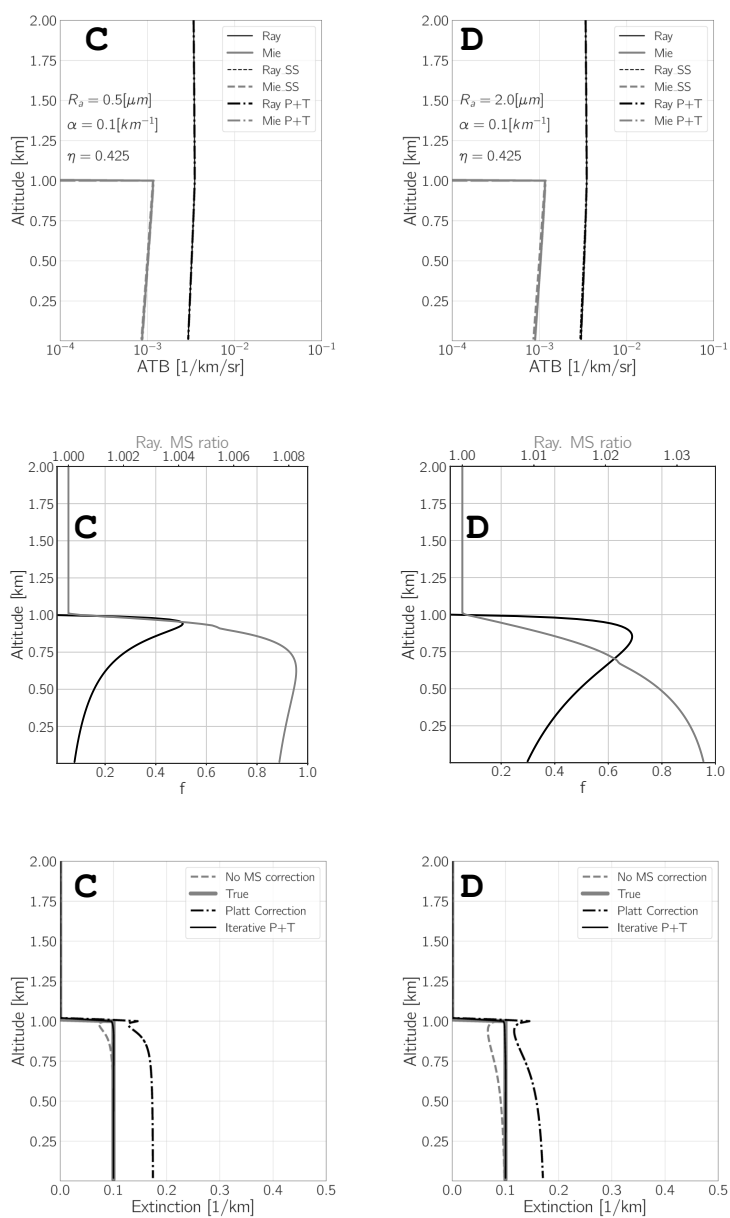
Figure B6. As Fig. B5 but for an extinction coefficient of 0.1 km^{-1} and $Ra = 0.5$ and $2[\mu m]$ respectively.
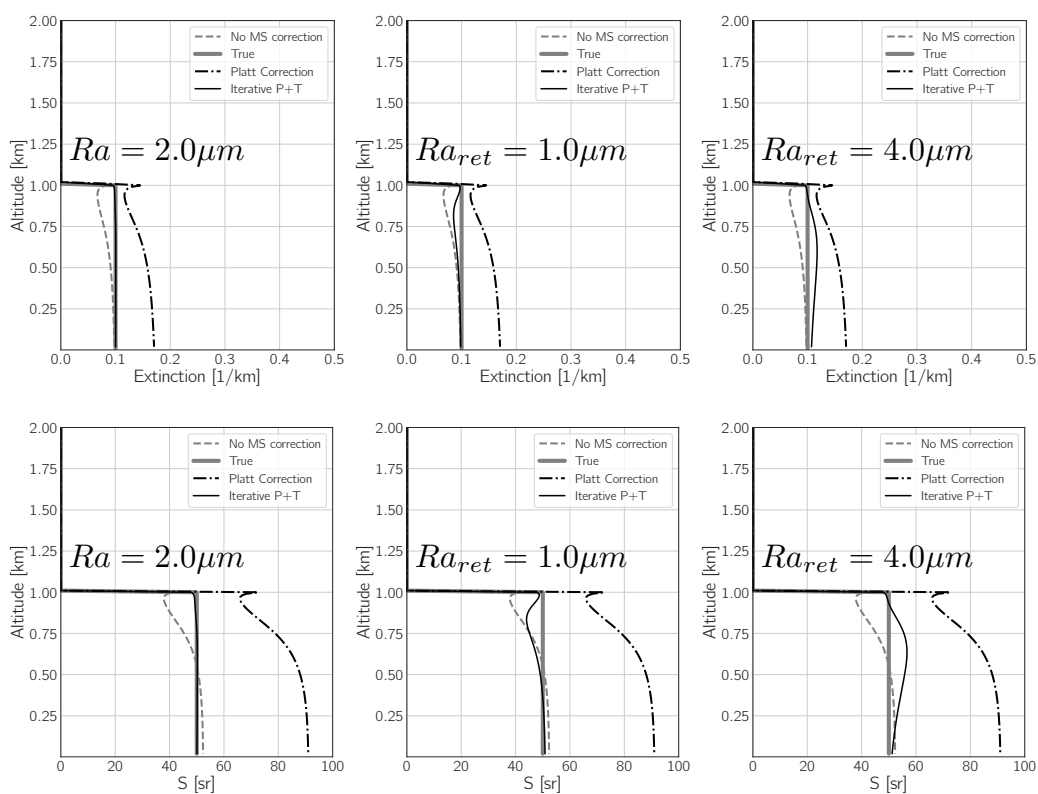
Figure B7. Top-panels extinction retrieved corresponding to the Case-D in Fig. B6 using the indicated values of Ra. The corresponding retrieved lidar-ratios are shown in the Bottom-panels.
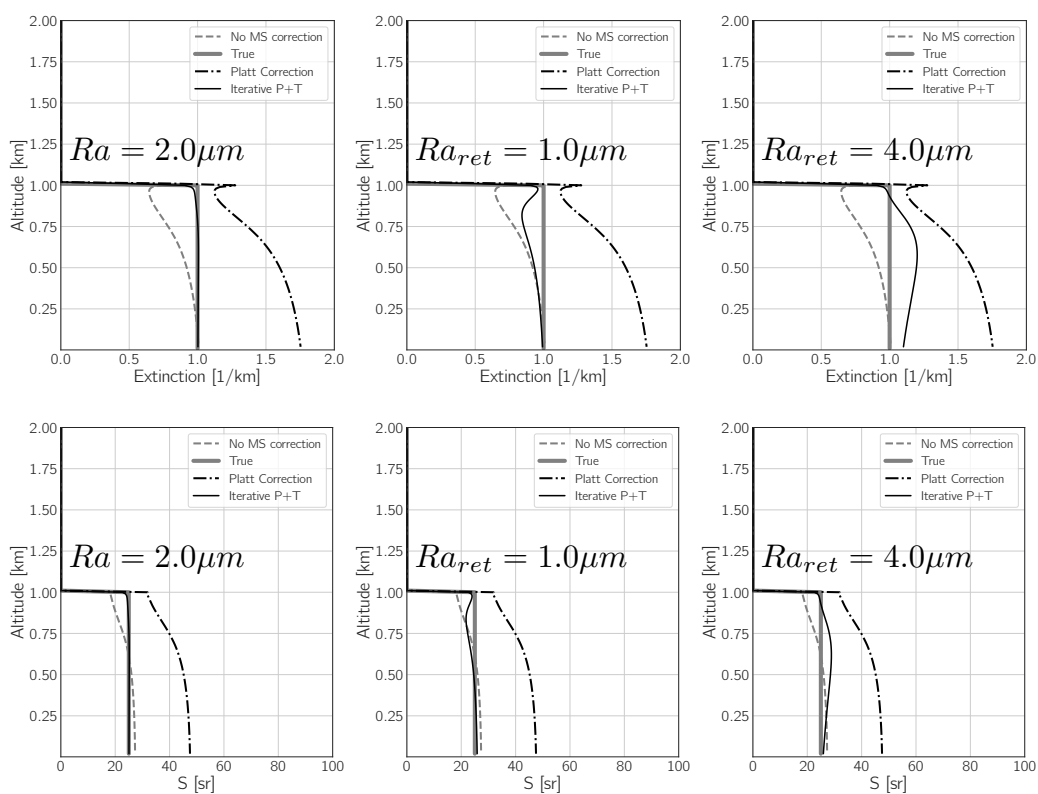
Figure B8. Top-panels extinction retrieved corresponding to the Case-A in Fig. B6 using the indicated values of Ra. The corresponding retrieved lidar-ratios are shown in the Bottom-panels.
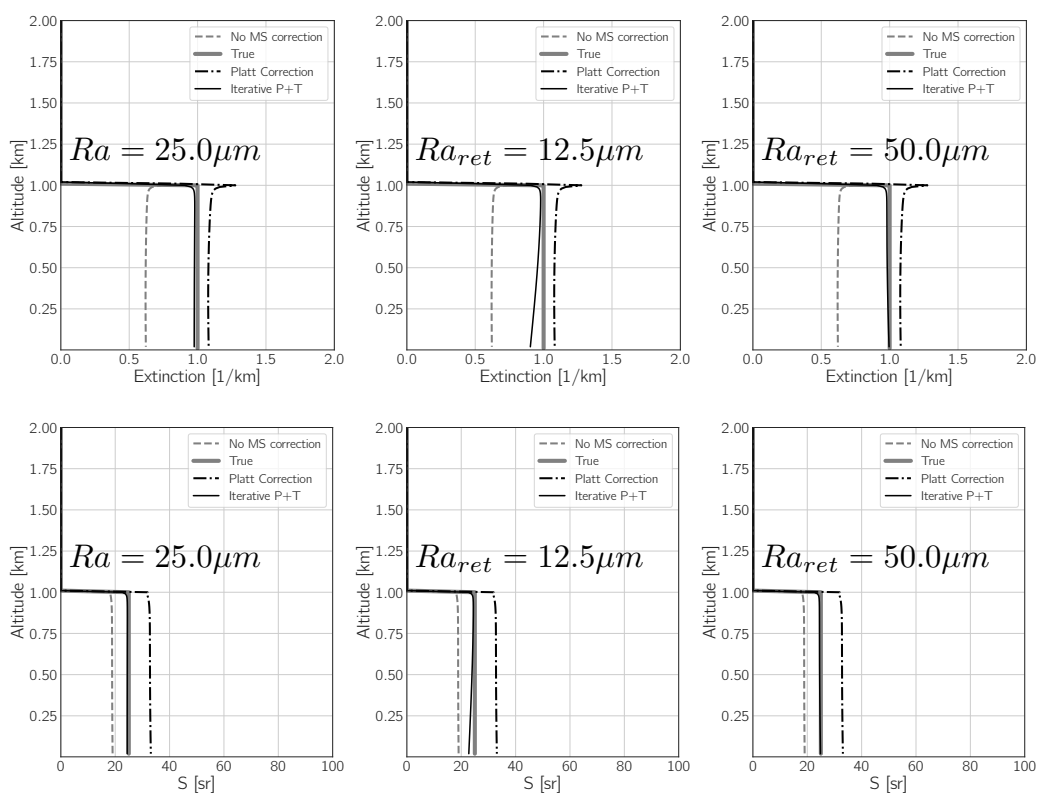
Figure B9. Top-panels extinction retrieved corresponding to the Case-B in Fig. B6 using the indicated values of Ra. The corresponding retrieved lidar-ratios are shown in the Bottom-panels.